Observable implications of geometrical and dynamical aspects of freeze-out in heavy ion collisions

Fabrice Retière[1] and Michael Annan Lisa[2]
[1]*Lawrence Berkeley National Laboratory, Berkeley, California 94720, USA*
[2]*Physics Department, The Ohio State University, Columbus, Ohio 43210, USA*
(Received 30 January 2004; published 29 October 2004)

Using an analytical parametrization of hadronic freeze-out in relativistic heavy ion collisions, we present a detailed study of the connections between features of the freeze-out configuration and physical observables. We focus especially on anisotropic freeze-out configurations (expected in general for collisions at finite impact parameter), azimuthally sensitive Hanburry-Brown-Twiss interferometry, and final-state interactions between nonidentical particles. Model calculations are compared with data taken in the first year of running at RHIC; while not perfect, good agreement is found, raising the hope that a consistent understanding of the full freeze-out scenario at RHIC is possible, an important first step towards understanding the physics of the system prior to freeze-out.

DOI: 10.1103/PhysRevC.70.044907 PACS number(s): 25.75.Ld, 25.75.Gz, 24.10.Nz

I. INTRODUCTION

The first data from collisions between heavy nuclei at the Relativistic Heavy Ion Collider (RHIC) have generated intense theoretical efforts to understand the hot, dense matter generated in the early stage of the collision [1]. Testing these theoretical ideas relies on comparison to experimental observables. Leptonic [2] or electromagnetic [3] observables are believed to probe directly the early, dense stage of the collision. Most of the early data from RHIC, however, have been on hadronic observables. Measurements of hadrons at high transverse momentum (p_T) [4] have generated much excitement, as they may provide useful *probes* of the dense medium produced at RHIC [5]. However, the medium *itself* decays largely into the soft (low-p_T) hadronic sector.

Soft hadronic observables measure directly the final "freeze-out" stage of the collision, when hadrons decouple from the bulk and free-stream to the detectors. Freeze-out may correspond to a complex configuration in the combined coordinate-momentum space, with collective components (often called "flow") generating space-momentum correlations, as well as geometrical and dynamical (flow) anisotropies. A detailed experimentally driven understanding of the freeze-out configuration is the crucial first step in understanding the system's prior evolution and the physics of hot colored matter.

In this paper, we explore in detail an analytic parametrization of the freeze-out configuration, which includes nontrivial correlations between coordinate- and momentum-space variables. We discuss the connections between the physical parameters of the model and observable quantities. If the model, with correct choice of physical model parameters, can adequately reproduce several independent measured quantities, then it might be claimed that this "crucial first step," mentioned above, has been performed.

A consistent reproduction of all low-p_T observations at RHIC is not achieved in most physical models which aim to describe the evolution of the collision. In particular, it is difficult to reproduce momentum-space measurements while simultaneously describing the freeze-out coordinate-space distribution probed by two-particle intensity interferometry measurements [6] [also known as Hanburry-Brown-Twiss (HBT) [7] measurements]. Hadronic cascade models predict a too weak momentum azimuthal anisotropy and too large source sizes [8]. Hydrodynamic transport models describe successfully transverse mass spectra and elliptic flow but fail at describing pion source radii [9]; some hydrodynamic models have successfully reproduced pion source radii [10], but only with different model parameters than those used to reproduce spectra and elliptic flow [11]. Similarly, sophisticated hybrid transport models (e.g., AMPT [12]) require different model parameters [13] to reproduce data on elliptic flow [15] and HBT measurements [16]. Good reproduction of observed values has been acheived in models which adjust parameters to fit data within a given freeze-out scenario, such as in the Buda-Lund hydro approach [17]. The work presented here falls into this latter category.

The parametrization used in this paper ("blast-wave parametrization") is similar in form to the freeze-out configuration obtained from hydrodynamic calculations [18], but we treat the physical parameters of the configuration (e.g., temperature) as free parameters. Our main goal is simply to quantify the driving physical parameters of freeze-out at RHIC and the dependence of observables on these parameters.

Further motivation for exploring freeze-out configurations of the type discussed here is that they implicitly assume a "bulk" system which may be described by global parameters (temperature, flow strength, etc.) Discussions of a "new phase of matter" and its "equation of state" are only sensible if indeed such assumptions hold. Comparison of blast-wave calculations with several independent measurements, then, is a crucial consistency check of these assumptions (though, of course, a successful comparison still would not constitute a proof of their validity).

In transport models, whether the constituents are hadrons [19,20], partons [21,22], or fluid elements [9,23–25], if they reinteract substantially, pressure gradients are generated,

leading to collective velocity fields ("flow"), pushing the matter away from the hot center of the collision and into the surrounding vacuum. Evidence of collective flow, generated by *final*-state reinteraction of collision products, has been based largely on interpretations of transverse mass spectra and transverse momentum azimuthal anisotropy [9]. However, this scenario has been challenged by new measurements of *p*-Au collisions [26] and new theoretical interpretations [27]. Indeed, so-called *initial*-state effects such as random walk of the incoming nucleons [26] or color glass condensate phenomena [27] may offer an alternative explanation of the measured spectra and anisotropies in transverse momentum. This ambiguity apparently threatens the concept that a *bulk* system has been created at all. However, it is important to recall that collective expansion, if it exists, would manifest itself not only in momentum-space observables, but would also generate space-momentum correlations, which can be measured via two-particle correlations.

The possible validity of any scenario may only be claimed if a single set of model parameters allows a successful description of *all* measured observables. Here, we study, in the context of a bulk collective flow scenario, transverse momentum spectra, momentum-space anisotropy ("elliptic flow"), HBT interferometry, and correlations between nonidentical particles.

Similar studies have been reported previously [25,28–31]. New aspects in our study include consideration of a more general (azimuthally anisotropic) freeze-out configuration, applicable to nonzero impact parameters; model studies of azimuthally sensitive HBT interferometry and correlations between nonidentical particles; and a multiobservable global fit to several pieces of published RHIC data.

This paper is organized as follows: In Sec. II, we describe the blast-wave parametrization. In Sec. III, we investigate in detail the sensitivity of several observables (p_T spectra, elliptic flow, pion HBT radii, and average space-time separation between different particle types) on the physical parameters of the blast-wave parametrization. In Sec. IV, we perform fits to published data measured at RHIC for Au+Au collisions at $\sqrt{s_{NN}}=130$ GeV and, based on these fits, describe how as-yet unpublished analyses (azimuthally sensitive HBT interferometry and correlations between nonidentical particles) are expected to look. The reader primarily interested in the quality of the fit to the data and the resulting parameters may want to skip past the details of Sec. III. In Sec. V, we summarize and conclude on the relevance of the blast-wave parametrization at RHIC.

II. BLAST-WAVE PARAMETRIZATION

A. Geneology and motivation

More than a quarter of a century ago, Westfall *et al.* [32] introduced the nuclear fireball model to explain midrapidity proton spectra. The idea was that the overlapping nucleons of the target and projectile combined to create a hot source with velocity between that of the target and projectile. Protons emitted from this source were expected to be emitted isotropically with a thermal energy distribution.

Soon thereafter, Bondorf, Garpman, and Zimanyi [33] derived a nonrelativistic expression for the energy spectra of particles emitted from a thermal *exploding* source. The radial flow in their (spherical) source results in energy spectra increasingly different than those from a purely thermal (nonflowing) source, as the particle mass increases. Siemens and Rasmussen [34] then generalized the formula with relativistic kinematics, further simplifying by assuming a single expanding radial shell.

While a spherically expanding source may be expected to approximate the fireball created in lower-energy collisions, at higher energies stronger longitudinal flow may lead to a cylindrical geometry. A decade ago, Schnedermann *et al.* [35] introduced a simple functional form for the phase-space density at kinetic freeze-out, which approximated hydrodynamical results assuming boost-invariant longitudinal flow [36], and successfully used it to fit p_T spectra with only two parameters: a kinetic temperature and a radial flow strength. The coordinate-space geometry was an infinitely long solid cylinder (and so should approximate the situation for $b=0$ collisions at midrapidity); the transverse radial flow strength necessarily vanished along the central axis and is assumed maximum at the radial edge. Most hydrodynamic calculations yield a transverse rapidity flow field linear in the radial coordinate [24].

Huovinen *et al.* [18] generalized this parametrization to account for the transversely anisotropic flow field which arises in *noncentral* collisions and which generates an elliptic flow signal similar to that seen in measurements [37]. This added one more parameter—the difference between the flow strength in and out of the reaction plane. The spatial geometry remained cylindrical, though it was assumed to be a cylindrical shell, not a solid cylinder.

The measured elliptical flow systematics as a function of p_T and mass are fairly well fit with the Huovinen parametrization [37]. However, better fits were achieved when the STAR Collaboration generalized the model even further, adding a fourth parameter designed to account for the anisotropic shape of the source in coordinate space [37]. A shell geometry was still assumed.

To calculate the spatial homogeneity lengths probed by two-particle correlation measurements [6], we must revert from the unrealistic shell geometry to a solid emission region (infinite series of elliptical shells). Furthermore, additional parameters corresponding to the source size, emission time, and emission duration must be included, increasing the number of parameters [38]. A similar generalization has been studied by Wiedemann [39]. Finally, in this paper, we explore the effects of a "hard-edge" versus a smooth spatial density profile; similar studies have recently been done by Tomášik *et al.* [40] and Peitzmann [30] for the more restricted case of a transversely isotropic source. This brings to 8 the total number of parameters which we study.

Although the blast-wave *functional form* was motivated by its similarity to the freeze-out configuration of a real dynamical model (i.e., hydrodynamical solutions), it is not necessarily true that the hydrodynamical freeze-out configuration corresponds to the parameter set that best describes the data. In this sense, the blast-wave model presented here remains only a parametrization. With eight freely tunable pa-

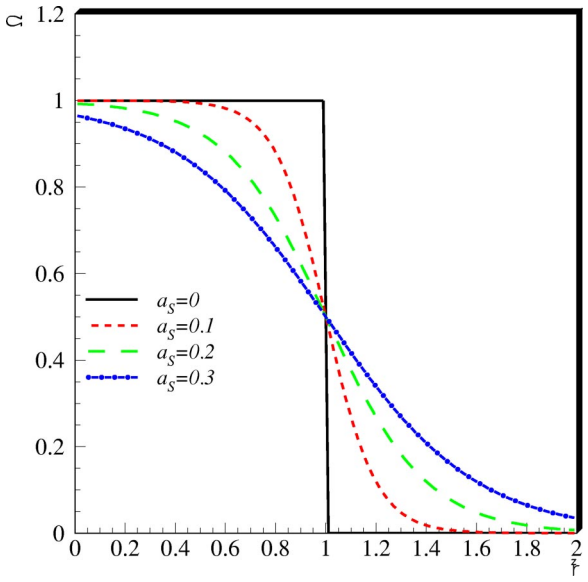

FIG. 1. (Color online) The source weighting function Ω as a function of the normalized elliptical radius $\tilde{r}$ for several values of the surface diffuseness parameter a_s.

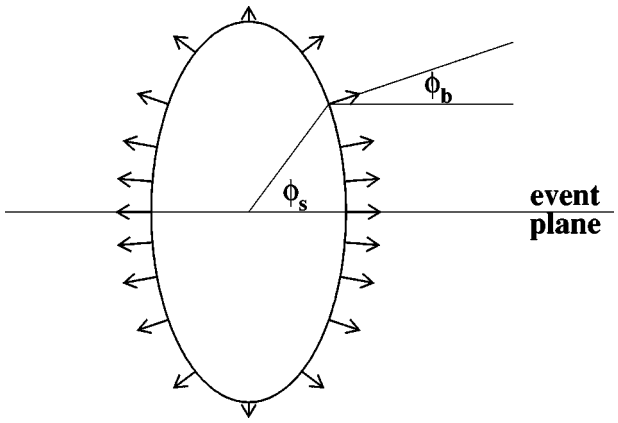

FIG. 2. Schematic illustration of an elliptical subshell of the source. Here, the source is extended out of the reaction plane ($R_y > R_x$). Arrows represent the direction and magnitude of the flow boost. In this example, $\rho_2 > 0$ [see Eq. (4)].

rameters, it is clearly a toy model with little predictive power. However, the goal is to see whether a consistent description of the data from the soft sector at RHIC is possible within a simple boost-invariant model with transverse collective flow. If this turns out to be the case, then it is worthwhile considering that the parameter values indeed characterize the size, shape, time scales, temperature, and flow strengths of the freeze-out configuration. A consistent parametrization in terms of such physical quantities represents a true step forward and provides valuable feedback to theorists constructing physical models of the collision.

B. Parameters and quantities in the blast wave

The eight parameters of the blast-wave parametrization described in this paper are T, ρ_0, ρ_2, R_y, R_x, a_s, τ_0, and $\Delta\tau$; their physical meaning is given below.

The freeze-out distribution is infinite in the beam (z) direction and elliptical in the transverse (x-y) plane. (The x-z plane is the reaction plane.) The transverse shape is controlled by the radii R_y and R_x, and the spatial weighting of source elements is given by

$$\Omega(r,\phi_s) = \Omega(\tilde{r}) = \frac{1}{1+e^{(\tilde{r}-1)/a_s}}, \tag{1}$$

where a fixed value of the "normalized elliptical radius,"

$$\tilde{r}(r,\phi_s) \equiv \sqrt{\frac{[r\cos(\phi_s)]^2}{R_x^2} + \frac{[r\sin(\phi_s)]^2}{R_y^2}}, \tag{2}$$

corresponds to a given elliptical subshell within the solid volume of the freeze-out distribution.

The parameter a_s corresponds to a surface diffuseness of the emission source. As shown in Fig. 1, a hard edge ("box profile") may be assumed by setting $a_s = 0$, while the density profile approximates a Gaussian shape for $a_s \approx 0.3$.

It should be noted that the weighting function $\Omega(r,\phi_s)$ is not, in general, the source density distribution. In particular, as we discuss especially in Secs. III C and III D, nonzero collective flow induces space-momentum correlations which dominate the spatial source density distributions. Only for a system without flow ($\rho_0 = \rho_2 = 0$; see below) is the source distribution given by Ω, so that, e.g., for $a_s = 0$, there is a uniform density of sources ($d^2N/dxdy = \text{const}$) inside the ellipse defined by R_y and R_x, and no sources outside.

The momentum spectrum of particles emitted from a source element at (x,y,z) is given by a fixed temperature T describing the thermal kinetic motion, boosted by a transverse rapidity $\rho(x,y)$. This is common in models of this type. However, unlike transversely *isotropic* parametrizations, the azimuthal direction of the boost (denoted ϕ_b) is *not* necessarily identical to the spatial azimuthal angle $\phi_s = \tan^{-1}(y/x)$. Instead, in our model, the boost is perpendicular to the elliptical subshell on which the source element is found; see Fig. 2. We believe this to be a more natural extension of an "outward" boost for nonisotropic source distributions than that used by Heinz and Wong [41], who used an anisotropic shape but always assumed radial boost direction ($\phi_b = \phi_s$). It may be shown that, for our model,

$$\tan(\phi_s) = \left(\frac{R_y}{R_x}\right)^2 \tan(\phi_b). \tag{3}$$

Hydrodynamical calculations for *central* collisions (i.e., azimuthally isotropic freezeout distribution) suggest that the flow rapidity boost depends linearly on the freeze-out radius [24]. We assume a similar scenario, but in our more generalized parametrization, the boost strength depends linearly on the normalized elliptical radius $\tilde{r}$ defined in Eq. (2). Thus, in the absence of an azimuthal dependence of the flow (to be introduced shortly), all source elements on the outer edge of the source boost with the same (maximum) transverse rapidity ρ_0 in an "outward" direction.

In noncentral collisions, the strength of the flow boost itself may depend on azimuthal angle, as suggested by

Huovinen *et al.* [18]. As those authors did, we incorporate this via a parameter ρ_2, which characterizes the strength of the second-order oscillation of the transverse rapidity as a function of ϕ_b. Hence, the flow rapidity is given by

$$\rho(r,\phi_s) = \tilde{r}[\rho_0 + \rho_2 \cos(2\phi_b)]. \tag{4}$$

We note that source anisotropy enters into our parametrization in two independent ways, and each contributes to, e.g., elliptic flow. Setting $\rho_2 > 0$ means the boost is stronger in plane than out of plane, contributing to positive elliptic flow. However, even if $\rho_2 = 0$ (but $\rho_0 \neq 0$), setting $R_y > R_x$ still generates positive elliptic flow, since this means there are *more* sources emitting in plane than out of plane (see Fig. 2). The STAR Collaboration found that both types of anisotropy were required to fit their elliptic flow data [37]. In generalizing the circular transverse geometry parametrization of Huovinen *et al.* [18] (in which $\phi_b = \phi_s$), they added a parameter s_2 and weighted source elements with a given ϕ_b as

$$\frac{dN}{d\phi_b} = \frac{dN}{d\phi_s} \sim [1 + 2s_2 \cos(2\phi_s)]. \tag{5}$$

Thus, a positive value of $s_2 = \langle \cos(2\phi_b) \rangle$ corresponded to more source elements emitting in plane, similar to setting $R_y > R_x$ in our parametrization.

To facilitate comparison of fits with the STAR model and with ours, we relate the s_2 of STAR to the geometric anisotropy of our parametrization. In the case of isotropic boost ($\rho_2 = 0$) [42],

$$s_2 = \langle \cos(2\phi_b) \rangle = \frac{1}{2} \frac{\left(\frac{R_y}{R_x}\right)^2 - 1}{\left(\frac{R_y}{R_x}\right)^2 + 1}. \tag{6}$$

If $\rho_2 \neq 0$, anisotropies in the space-momentum correlations lead to a significantly more complicated expression.

Finally, since our model is based on a longitudinally boost-invariant assumption, it is sensible that the freeze-out occurs with a given distribution in longitudinal proper time $\tau = \sqrt{t^2 - z^2}$. We assume a Gaussian distribution peaked at τ_0 and with a width $\Delta\tau$:

$$\frac{dN}{d\tau} \sim \exp\left(- \frac{(\tau - \tau_0)^2}{2\Delta\tau^2} \right). \tag{7}$$

We note that although the source emits particles over a finite duration in proper time τ, we assume that none of the source parameters changes with τ. This is obviously an oversimplification valid only for small $\Delta\tau$; with time, one may expect the flow field to evolve (increase *or* decrease), and it is natural to expect the transverse sizes R_x and R_y to change (grow *or* fall) with time. However, calculation of the time dependence of these parameters requires a true dynamical model and is outside the scope and spirit of the present work.

C. Emission function

Our emission function is essentially a generalization of azimuthally isotropic emission functions used by previous authors [43–46], and here we follow closely [44]:

$$\begin{aligned} S(x,K) &= m_T \cosh(\eta - Y) \Omega(r,\phi_s) e^{-(\tau - \tau_0)^2/2\Delta\tau^2} \frac{1}{e^{K\cdot u/T} \pm 1} \\ &= m_T \cosh(\eta - Y) \Omega(r,\phi_s) e^{-(\tau - \tau_0)^2/2\Delta\tau^2} \\ &\quad \times \sum_{n=1}^{\infty} (\mp 1)^{n+1} e^{-nK\cdot u/T}, \end{aligned} \tag{8}$$

where the upper (lower) sign is for fermions (bosons). Often, only the first term in the sum in Eq. (8) is used, resulting in a Boltzmann distribution for all particles. Below, we show that there is a small change to observables when truncating after the second term and negligible effect when including further terms. The Boltzmann factor $\exp(-K\cdot u/T)$ arises from our assumption of local thermal equilibrium within a source moving with four-velocity $u_\mu(x)$. We assume longitudinal boost invariance by setting the longitudinal flow velocity $v_L = z/t$ ($z = \tau \sinh \eta$ and $t = \tau \cosh \eta$), so that the longitudinal flow rapidity $\eta_{\text{flow}} = \frac{1}{2}\ln[(1+v_L)/(1-v_L)]$ is identical [36] to the space-time rapidity $\eta = \frac{1}{2}\ln[(t+z)/(t-z)]$. Thus, in cylindrical coordinates,

$$\begin{aligned} u_\mu(x) = (&\cosh \eta \cosh \rho(r,\phi_s), \sinh \rho(r,\phi_s) \cos \phi_b, \\ &\sinh \rho(r,\phi_s) \sin \phi_b, \sinh \eta \cosh \rho(r,\phi_s)) \end{aligned} \tag{9}$$

and

$$K_\mu = (m_T \cosh Y, p_T \cos \phi_p, p_T \sin \phi_p, m_T \sinh Y), \tag{10}$$

where the transverse momentum (p_T), transverse mass (m_T), rapidity (Y), and azimuthal angle (ϕ_p) refer to the *momentum of the emitted particle*, not the source element. (Note that three azimuthal angles ϕ_s, ϕ_b, and ϕ_p are relevant to this discussion.) Thus,

$$\begin{aligned} K_\mu u^\mu = &m_T \cosh \rho(r,\phi_s) \cosh(\eta - Y) \\ &- p_T \sinh \rho(r,\phi_s) \cos(\phi_b - \phi_p), \end{aligned} \tag{11}$$

and the emission function [Eq. (8)] may be rewritten as

$$\begin{aligned} S(x,K) = S(r,\phi_s,\tau,\eta) &= m_T \cosh(\eta - Y) \Omega(r,\phi_s) e^{-(\tau - \tau_0)^2/2\Delta\tau^2} \\ &\times \sum_{n=1}^{\infty} (\mp 1)^{n+1} e^{n\alpha \cos(\phi_b - \phi_p)} e^{-n\beta \cosh(\eta - Y)}, \end{aligned} \tag{12}$$

where we define

$$\alpha \equiv \frac{p_T}{T} \sinh \rho(r,\phi_s), \tag{13}$$

$$\beta \equiv \frac{m_T}{T} \cosh \rho(r,\phi_s). \tag{14}$$

Exploiting the boost invariance and infinite longitudinal extension of our source and focusing on observables at midrapidity and using the longitudinally comoving system (LCMS) for HBT measurements, we may simplify Eq. (12) by setting $Y = 0$.

D. Calculating observables

All observables which we will calculate are related to integrals of the emission function (12) over phase space $d^4x = dxdydzdt = \tau d\tau d\eta r dr d\phi_s$, weighted with some quantity $B(x,K)$. In all cases, the integrals over τ and η may be done analytically, though the result depends on whether $B(x,K)$ itself depends on τ and η.

In particular, if $B(x,K) = B'(r,\phi_s,K)\tau^j \sinh^j\eta \cosh^k\eta$, then the integrals of interest are [47]

$$\int_0^{2\pi} d\phi_s \int_0^{\infty} r dr \int_{-\infty}^{\infty} d\eta \int_{-\infty}^{\infty} \tau d\tau S(x,K) B(x,K) = m_T H_i \{B'\}_{j,k}(K), \tag{15}$$

where the τ and η integrals are denoted

$$H_i \equiv \int_{-\infty}^{\infty} d\tau \tau^{j+1} e^{-(\tau-\tau_0)^2/2\Delta\tau^2},$$

$$H_0 = \sqrt{2\pi}\,\Delta\tau\,\tau_0,$$

$$H_1 = \sqrt{2\pi}\,\Delta\tau(\Delta\tau^2 + \tau_0^2),$$

$$H_2 = \sqrt{2\pi}\,\Delta\tau\,\tau_0(3\Delta\tau^2 + \tau_0^2) \tag{16}$$

and

$$G_{j,k}(x,K) \equiv \int_{-\infty}^{\infty} d\eta e^{-\beta\cosh\eta} \sinh^j\eta \cosh^{k+1}\eta,$$

$$G_{0,0}(x,K) = 2\mathrm{K}_1(\beta),$$

$$G_{0,1}(x,K) = 2\left[\frac{\mathrm{K}_1(\beta)}{\beta} + \mathrm{K}_0(\beta)\right],$$

$$G_{1,0}(x,K) = G_{1,1}(x,K) = 0,$$

$$G_{0,2}(x,K) = 2\left[\frac{\mathrm{K}_2(\beta)}{\beta} + \mathrm{K}_1(\beta)\right],$$

$$G_{2,0}(x,K) = 2\frac{\mathrm{K}_2(\beta)}{\beta}. \tag{17}$$

β was defined in (14), and K_n are the modified Bessel functions. For the above, we define the notation

$$\{B'\}_{j,k}(K) \equiv \sum_{n=1}^{\infty}\left\{(\mp 1)^{n+1}\int_0^{2\pi} d\phi_s \times \int_0^{\infty} r dr [G_{j,k}(x,nK)B'(x,K) \times e^{n\alpha\cos(\phi_b-\phi_p)}\Omega(r,\phi_s)]\right\} \tag{18}$$

for the remaining integrals, which we perform numerically. [Note that $G_{i,j}(x,nK)$ retains dependence on r and ϕ_s due to its dependence on β, as defined in Eq. (14), and so cannot move outside the integrals in Eq. (18).]

TABLE I. Default parameter values for most calculations in Sec. III. Note that ρ_2, R_x, and R_y default values depend on whether we are discussing an azimuthally isotropic ("round") or anisotropic ("nonround") source. One might expect such sources from central and peripheral collisions, respectively.

Parameter	Round source	Nonround source
ρ_2	0	0.05
R_x (fm)	12.04	11
R_y (fm)	12.04	13
T (GeV)	0.1	
ρ_0	0.9	
τ_0 (fm/c)	9	
$\Delta\tau$ (fm/c)	2	
a_s	0	

III. CALCULATION OF HADRONIC OBSERVABLES

In this section, we discuss how hadronic observables are calculated from the parametrized source and illustrate the sensitivity of these observables to the various parameters presented in Sec. II B.

With several observables depending on several parameters, it is not feasible to explore the entire numerical parameter space. Instead, we anticipate the results of the next section, in which we fit our model to existing data, and vary the parameters by "reasonable" amounts about values similar to those which fit the data. The default parameter values used in several of the calculations in this section are listed in Table I.

A. p_T spectra

In the notation of Sec. II D the (azimuthally integrated) p_T spectrum is calculated as

$$\frac{dN}{p_T dp_T} = \int d\phi_p \int d^4x S(x,K) \propto m_T \int d\phi_p \{1\}_{0,0}(K). \tag{19}$$

In this paper, we focus only on the shapes, not the normalizations, of the spectra.

We note that spectra calculated in the blast-wave model scale neither with m_T nor p_T, as both quantities enter the expression through α and β [Eqs. (13) and (14)]. This breaking of m_T scaling is a well-known consequence of finite transverse flow [35] ($\rho \neq 0$ in our model).

According to Eq. (19), m_T spectra calculated in the blast-wave model are insensitive to the time parameters τ_0 and $\Delta\tau$. The spectral shapes are furthermore insensitive to the spatial scale (i.e., R_y) of the source, though, as we see below, there is some small sensitivity to the spatial shape (i.e., R_y/R_x).

First, we study the importance of using quantum (as opposed to classical) statistics in the source function. Figure 3 shows p_T spectra for pions and protons, treated as bosons and

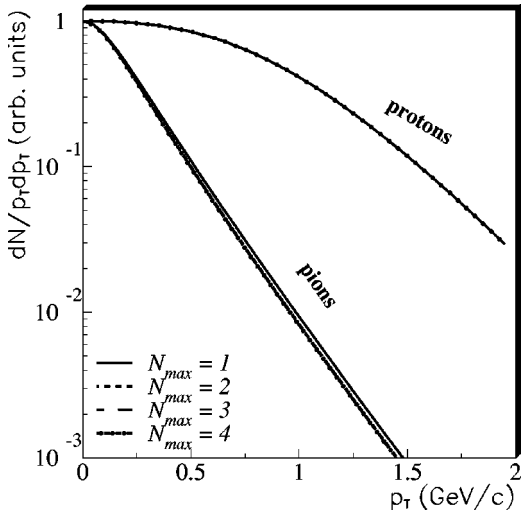

FIG. 3. Transverse momentum spectra for protons (upper curves) and pions (lower curves), as calculated by Eq. (19), for several values of N, the maximum value of n taken in the summation of Eq. (8); see text for details. Parameter values correspond to the "nonround" source of Table I. All spectra are arbitrarily normalized to unity at $p_T=0$.

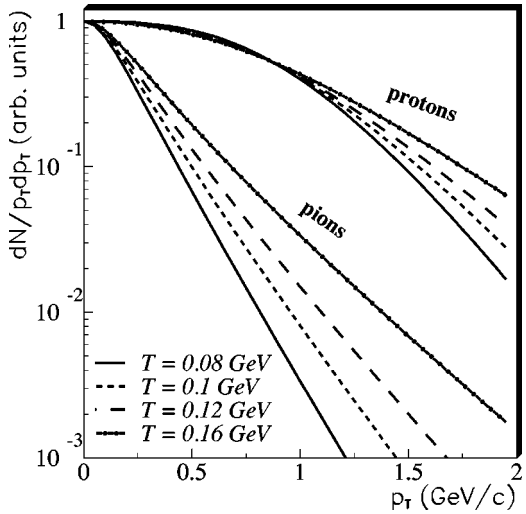

FIG. 4. Transverse momentum spectra for protons (upper curves) and pions (lower curves), as calculated by Eq. (19), for several values of the temperature parameter T. Other parameters follow the "round" source defaults of Table I. All spectra are arbitrarily normalized to unity at $p_T=0$.

fermions, respectively. Model parameters were set to the "nonround" values listed in Table I. The sum in Eq. (8) [and Eqs. (12) and (18)] is over $n=1,\ldots,N$; curves are shown for $N=1,2,3,4$. For parameter values in the range we study here, proton spectra are essentially independent of N. For $N>1$, the pion spectra are likewise robust against the value of N, though in the classical limit ($N=1$), there is relatively lower yield at low p_T. (Note that all spectra are arbitrarily normalized to unity at $p_T=0$.) Calculations below use the truncation $N=2$.

1. Spectra from central collisions

Focusing first on central collisions (so that the flow anisotropy parameter $\rho_2=0$ and $R_x=R_y$), then, we need only consider the spectra sensitivity to the temperature and radial flow parameters ρ_0 and T, and to the surface diffusion a_s.

Fixing the transverse spatial density distribution to a box profile ($a_s=0$), the evolution of spectral shapes for pions and protons are shown in Figs. 4 and 5, as the temperature and radial flow parameter, respectively, are varied about nominal values of $T=100$ MeV and $\rho_0=0.9$. As has been noted previously [35], at low p_T, temperature variations affect the lighter pions more strongly, while variations in the collective flow boost produce a stronger effect on the heavier particles.

Next, we consider the effect of a finite surface diffuseness parameter ($a_s\neq 0$)—i.e., using the smoother spatial density distributions of Fig. 1. Since we assume a transverse flow profile which increases linearly with radius [cf. Eq. (4)], one trivial effect is that, for a fixed ρ_0, increasing a_s will produce a larger average flow boost $\langle\rho\rangle$. The effect of increasing transverse flow was already explored directly in Fig. 5, so we avoid this trivial effect here, and explore the effect of varying a_s, while keeping $\langle\rho\rangle$ constant [30].

The average transverse flow boost $\langle\rho\rangle=F(a_s)\rho_0$ where the geometric proportionality constant

$$F(a_s)=\frac{\displaystyle\int_0^\infty dx\frac{x^2}{1+\exp[(x-1)/a_s]}}{\displaystyle\int_0^\infty dx\frac{x}{1+\exp[(x-1)/a_s]}} \tag{20}$$

is independent of ρ_0 or $R=R_x=R_y$. For the box profile, $F(a_s=0)=\frac{2}{3}$. Figure 6 shows this geometric factor as a function of the surface diffuseness.

Figure 7 shows the pion and proton spectra for various values of a_s. The radial flow strength ρ_0 was covaried with a_s so that the average transverse flow boost was $\langle\rho\rangle=0.6$. To a

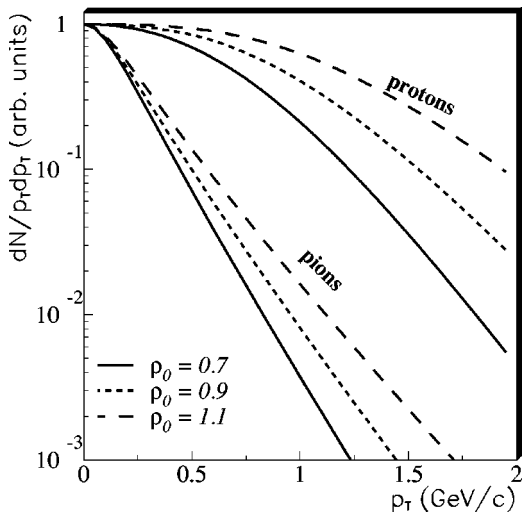

FIG. 5. Transverse momentum spectra for protons (upper curves) and pions (lower curves), as calculated by Eq. (19), for several values of the radial flow parameter ρ_0. Other parameters follow the "round" source defaults of Table I. All spectra are arbitrarily normalized to unity at $p_T=0$.

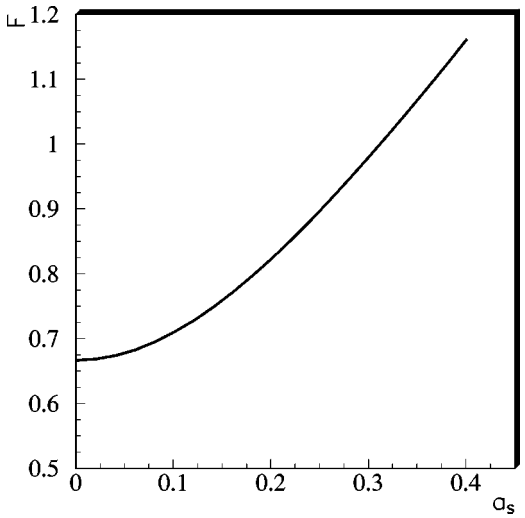

FIG. 6. The geometric constant of proportionality F between the average transverse flow boost $\langle\rho\rangle$ and the blast-wave parameter ρ_0, as a function of the surface diffuseness a_s.

first approximation, the spectral shapes depend only on the temperature T and the average transverse flow boost $\langle\rho\rangle$. The residual dependence on the surface diffuseness parameter a_s arises from the fact that while the *average* boost rapidity has been held constant, the *spread* of boost rapidities increases with increasing a_s [30]. Thus, we observe *qualitatively* similar variations in the spectral shapes when a_s increases (Fig. 7), as when T increases (Fig. 4). The variations are not *quantitatively* identical since in the present case, the velocity spread is not thermal, and the particle velocity spread evolves differently with mass, depending on whether it arises from a boost spread or a thermal spread.

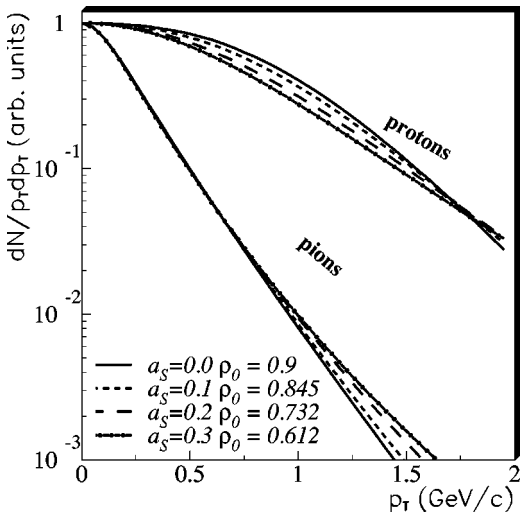

FIG. 7. Transverse momentum spectra for protons (upper curves) and pions (lower curves), as calculated by Eq. (19), for several values of the surface diffuseness parameter a_s. The radial flow strength ρ_0 is covaried; see text for details. Other parameters follow the "round" source defaults of Table I. All spectra are arbitrarily normalized to unity at $p_T=0$.

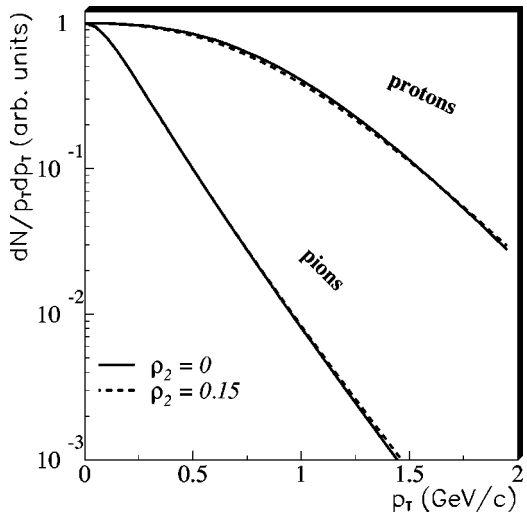

FIG. 8. Transverse momentum spectra for protons (upper curves) and pions (lower curves), as calculated by Eq. (19) for an azimuthally symmetric flow field ($\rho_2=0$) and an asymmetric field ($\rho_2=0.15$). Other parameters follow the "round" source defaults of Table I. All spectra are arbitrarily normalized to unity at $p_T=0$.

2. Dependence of spectral shapes on source anisotropy

Azimuthally integrated p_T spectra are often presented as a function of event centrality. For $b\neq 0$ collisions, the emitting source may have anisotropic structure ($R_x\neq R_y$ and $\rho_2\neq 0$ in the present model). Thus, it is interesting to explore possible effects of these anisotropies.

For an azimuthally isotropic flow field ($\rho_2=0$), the spectral shapes are insensitive to spatial anisotropies in the source (i.e., $R_x\neq R_y$). This is because the spectral shapes are determined by the distribution of boost velocities [30], which is unchanged by a shape change in our parametrization, if $\rho_2=0$.

For an azimuthally symmetric spatial source ($R_x=R_y$), a very small variation in the ϕ_p-integrated spectral shapes is observed when ρ_2 is changed from a value of 0.0 to 0.15, as seen in Fig. 8. This, again, is due to the slightly increased spread in boost velocities; source elements emitting in plane boost a bit more and out of plane a bit less. This effect becomes stronger in the presence of an out-of-plane spatial anisotropy ($R_y/R_x>1$) as shown in Fig. 9. In any case, the effects of "reasonable" source anisotropy on the shapes of azimuthally integrated spectra are very small.

Thus, we conclude that azimuthally integrated p_T spectra are largely insensitive to "reasonable" source anisotropies (see Sec. IV for "reasonable" ranges) and probe mainly the thermal motion (T) and average transverse flow boost ($\langle\rho\rangle$) of the source.

B. Elliptic flow versus mass and p_T

In the notation of Sec. II D the elliptic flow parameter v_2 is calculated as

$$v_2(p_T,m)=\frac{\int_0^{2\pi} d\phi_p\{\cos(2\phi_p)\}_{0,0}(K)}{\int_0^{2\pi} d\phi_p\{1\}_{0,0}(K)}. \qquad (21)$$

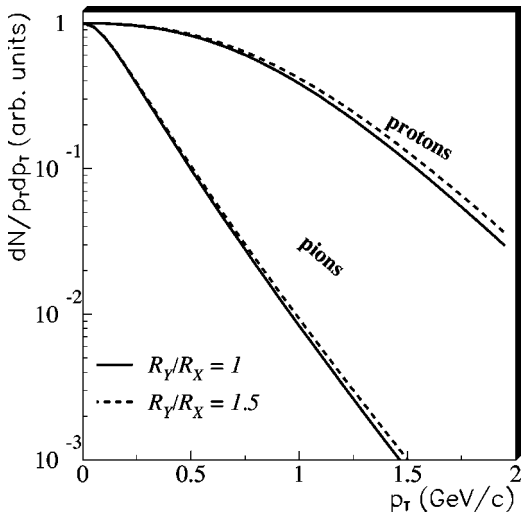

FIG. 9. Transverse momentum spectra for protons (upper curves) and pions (lower curves), as calculated by Eq. (19) for an azimuthally anisotropic flow field ($\rho_2=0.15$) and a spatially isotropic ($R_y/R_x=1$) and anisotropic ($R_y/R_x=1.5$) spatial distribution. Other parameters follow the "round" source defaults of Table I.

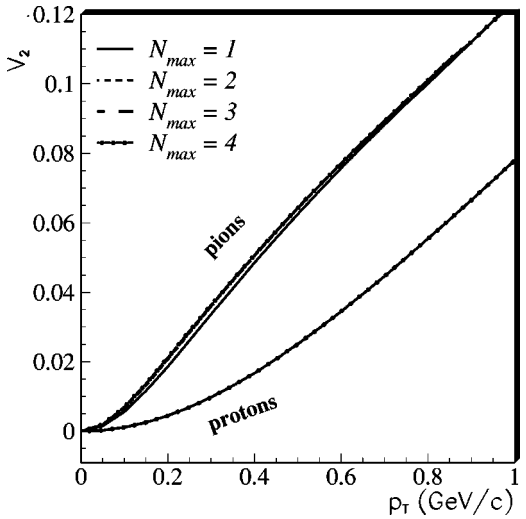

FIG. 10. Elliptic flow parameter v_2 for pions (upper curves) and protons (lower curves), as a function of transverse momentum, as calculated by Eq. (21), for several values of N, the maximum value of n taken in the summation of Eq. (8); see text for details. Model parameters follow the "nonround" source defaults of Table I.

A finite v_2 arises from azimuthal anisotropies in the source ($R_x \neq R_y$ and/or $\rho_2 \neq 0$). As discussed below, however, the parameters ρ_0 and T strongly affect its value and evolution with p_T and mass. In the present parametrization, v_2 is not sensitive to the overall spatial scale of the source (R_y) or the time parameters τ_0 and $\Delta\tau$.

The v_2 parameter depends nontrivially on both p_T and particle mass [18,37,48,49]. In this section, we explore the evolution of pion and proton v_2, as we vary the model parameters from nominal "nonround" values for noncentral collisions (cf. Sec. I).

As with the p_T spectra of Sec. III A, we first check the importance of quantum statistics. Figure 10 shows v_2 for pions and protons, for different values of N, where the sum in Eq. (8) [and Eqs. (12) and (18)] runs over $n=1,\ldots,N$. Again, we find only a small difference for the pions between $N=1$ (classical limit) and $N=2$, beyond which v_2 is robust against further increases in N. Calculations here use $N=2$.

Figure 11 shows the evolution of v_2 as the temperature parameter (T) is varied. For both particle types shown, the increased thermal smearing in momentum space, as T is increased, leads to a reduced momentum-space anisotropy. The effect of the thermal smearing is greater for the lighter pions.

Less intuitive is the evolution of v_2 as the flow field (ρ_0 or ρ_2) is varied. In Figs. 12 and 13, the average transverse flow parameter ρ_0 is varied for an azimuthally isotropic ($R_y/R_x=1$) and anisotropic ($R_y/R_x=13/11$) shape, respectively. For the isotropic spatial distribution, we find that v_2 decreases as ρ_0 increases, for all p_T and for both particle types. This is due to the decreasing relative amplitude of the oscillation in the flow field. Not surprisingly, the effect is larger for the heavier protons.

Indeed, it has been pointed out [18,49,50] that high radial flow (large ρ_0) can lead to negative values of v_2 for heavy particles; this is clearly true for the protons in Fig. 12. This negative v_2 reflects the *depletion* of the low-p_T particle yield when most source elements are highly boosted transversely; this is also the origin of the "shoulder arm" in the p_T spectra (cf. Sec. III A). This depletion is larger in plane (since the boost is higher—i.e., $\rho_2>0$), leading to negative v_2. At higher p_T and/or lower flow strengths, the competing effect is dominant: the larger in-plane boost leads to more particles emitted in plane, and $v_2>0$.

For a slightly anisotropic shape ($R_y/R_x=13/11$, Fig. 13), the v_2 parameter increases significantly for both protons and pions, due to the larger number of source elements boosted in plane (cf. Fig. 2). The finite spatial asymmetry leads to an effect that tends to oppose the reduction of v_2 with increasing

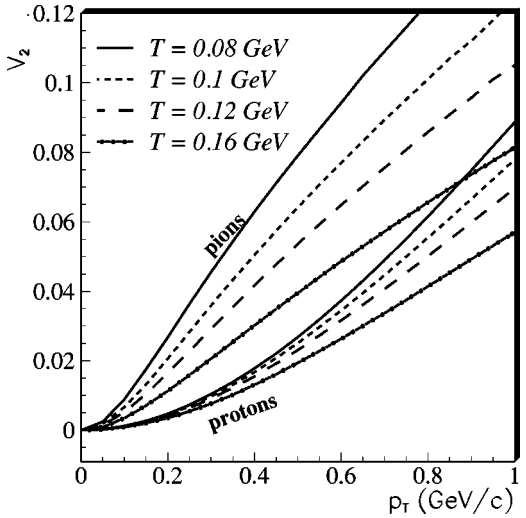

FIG. 11. Elliptic flow parameter v_2 for pions (upper curves) and protons (lower curves), as a function of transverse momentum, as calculated by Eq. (21), for various values of the temperature parameter T. Other parameters follow the "nonround" source defaults of Table I.

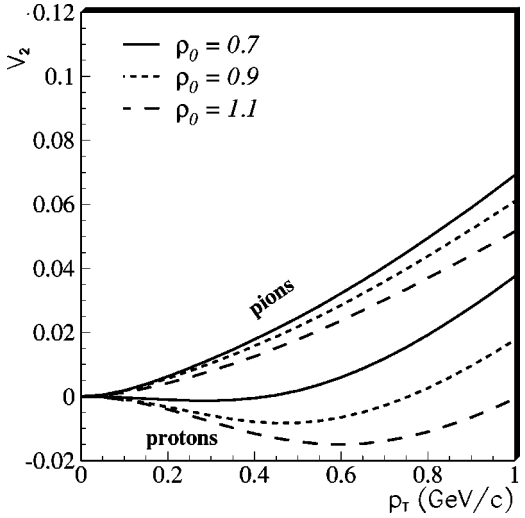

FIG. 12. Elliptic flow parameter v_2 for pions (upper curves) and protons (lower curves), as a function of transverse momentum, as calculated by Eq. (21), for various values of the transverse flow parameter ρ_0. The source spatial distribution is assumed azimuthally anisotropic ($R_y = R_x$), but other parameters follow the "nonround" source defaults of Table I.

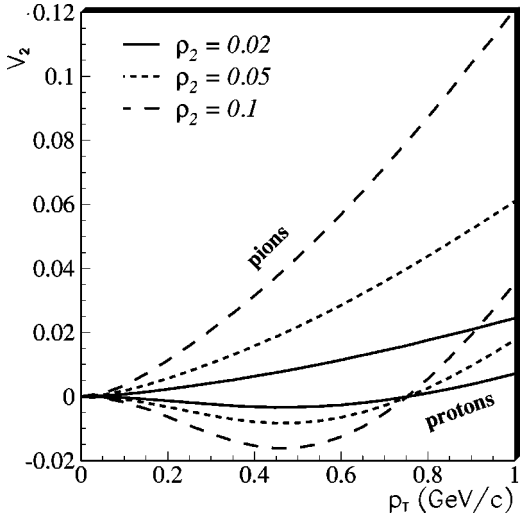

FIG. 14. Elliptic flow parameter v_2 for pions (upper curves) and protons (lower curves), as a function of transverse momentum, as calculated by Eq. (21), for various values of the modulation in the transverse flow ρ_2. Other parameters follow the *"round"* (note that $R_y = R_x$) source defaults of Table I.

ρ_0, discussed above and, for pions at low p_T, even reverses it in this case. Hence, at low p_T, increasing ρ_0 increases (decreases) v_2 for pions (protons).

We observe similar trends when ρ_0 is held fixed and ρ_2 is varied. Figure 14 shows v_2 evolution for a spatially azimuthally symmetric source ($R_y/R_x = 1$) and Fig. 15 for a slightly asymmetric source ($R_y/R_x = 13/11$).

As mentioned above, a finite value of v_2 may be obtained for an azimuthally *symmetric* flow field if the spatial shape is asymmetric. Figure 16 shows the proton and pion v_2 for $\rho_2 = 0$ and $\rho_0 = 0.9$, for various values of R_y/R_x. The larger number of sources emitting in plane results in more particles measured in plane (thus $v_2 > 0$). This momentum-space asymmetry saturates at $p_T \sim 1.0$ GeV/c (for this set of parameters) and is relatively independent of particle mass. (We note that the p_T scale in Fig. 16 is larger than the other figures, in order to show the v_2 saturation effect.) This effect is similar to those previously discussed by Houvinen *et al.* [51] and Shuryak [52]. However, we stress that the nonzero v_2 parameter does *not* indicate "elliptic flow without transverse flow," as suggested in [51]. If transverse flow is turned off ($\rho_0 = 0$), the spectra are thermal and isotropic, and $v_2 = 0$ for all p_T; space-momentum correlations (induced by $\rho \neq 0$ in

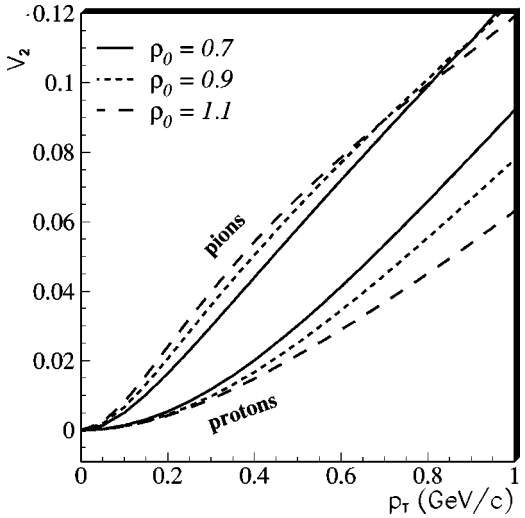

FIG. 13. Elliptic flow parameter v_2 for pions (upper curves) and protons (lower curves), as a function of transverse momentum, as calculated by Eq. (21), for various values of the transverse flow parameter ρ_0. Other parameters follow the "nonround" source defaults of Table I.

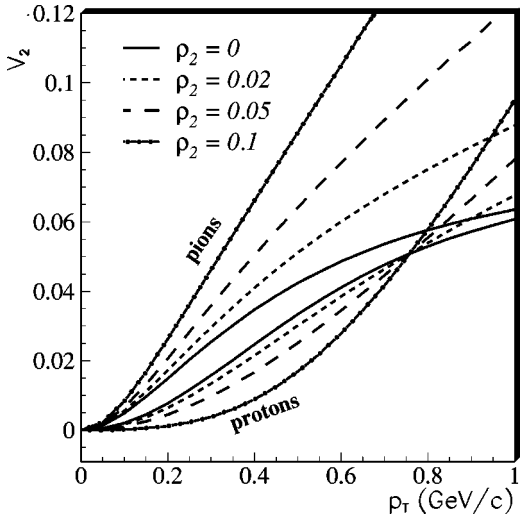

FIG. 15. Elliptic flow parameter v_2 for pions (upper curves) and protons (lower curves), as a function of transverse momentum, as calculated by Eq. (21), for various values of the modulation in the transverse flow ρ_2. Other parameters follow the "nonround" source defaults of Table I.

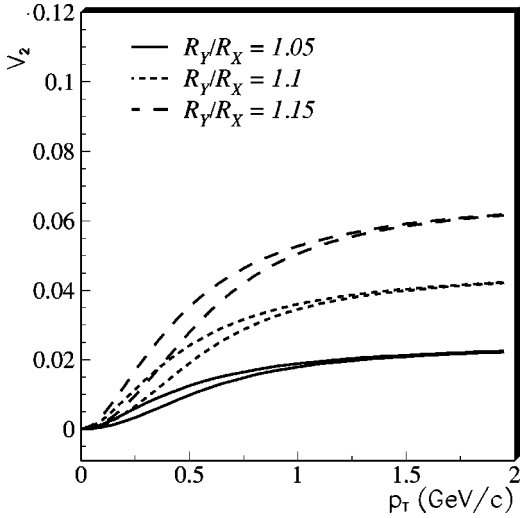

FIG. 16. Elliptic flow parameter v_2 for pions (upper curves) and protons (lower curves), as a function of transverse momentum, as calculated by Eq. (21), for various values of the spatial anisotropy (R_y/R_x). Elliptic flow parameter v_2 for pions (upper curves) and protons (lower curves), as a function of transverse momentum, as calculated by Eq. (21), for various values of the modulation in the transverse flow ρ_2. Other parameters follow the "*round*" (note that $\rho_2=0$) source defaults of Table I.

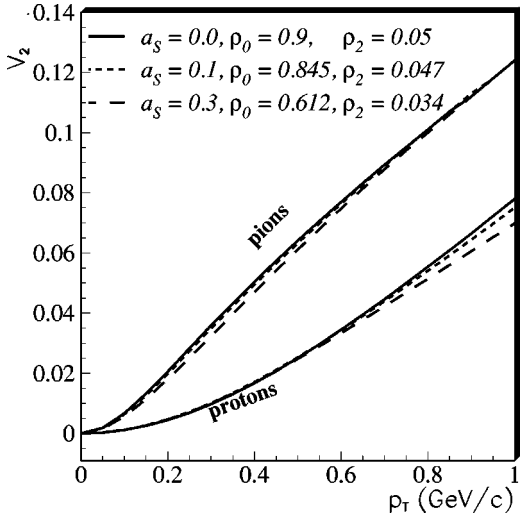

FIG. 17. Elliptic flow parameter v_2 for pions (upper curves) and protons (lower curves), as a function of transverse momentum, as calculated by Eq. (21), for various values of the surface diffuseness parameter a_s. The values of ρ_0 and ρ_2 are covaried with a_s so that the average transverse flow and its average azimuthal modulation remain fixed; see text. Other parameters follow the "nonround" source defaults of Table I.

our model) are required for a finite v_2. In the model of Houvinen *et al.* [51] it is the implementation of the Cooper-Frye freeze-out procedure (which creates an infinitely opaque source) which produces the space-momentum correlations, effectively generating "flow." Shuryak [52] implemented a parameter κ which controlled the opaqueness; v_2 was found to increase with κ until the source was essentially infinitely opaque.

Finally, we again explore the effect of "softening" the spatial source distribution $\Omega(r,\phi_s)$. Similar to the discussion surrounding Fig. 7, it is clear that the most meaningful comparison comes from keeping the average value of the transverse boost (and its anisotropy) constant, not keeping the parameters ρ_0 and ρ_2 constant, as we vary a_s. Similar to the discussion of the p_T spectra, we find in Fig. 17 that v_2 is largely insensitive to the surface diffuseness parameter a_s.

C. HBT radii versus p_T and ϕ_p

The previous subsections have discussed momentum-space observables only, even though coordinate-space considerations came into play indirectly. The most direct experimental probes of the space-time structure of the freeze-out configuration are two-particle correlation functions in relative momentum [6,53]. Here, we use the standard "out-side-long" coordinate system of Pratt *et al.* [54] and Bertsch *et al.* [54], in which the long direction (R_l) is parallel to the beam, the side direction (R_s) is perpendicular to the beam and total pair momentum, and the out direction (R_o) is perpendicular to the long and side directions.

For boost-invariant sources, the HBT radii R_{ol}^2 and R_{sl}^2 vanish by symmetry [55]. (For the more general case, see Refs. [39,55–58].) Thus, we are left with four HBT radii, which are related to space-time variances as [6,39]

$$R_s^2 = \frac{1}{2}(\langle\tilde{x}^2\rangle + \langle\tilde{y}^2\rangle) - \frac{1}{2}(\langle\tilde{x}^2\rangle - \langle\tilde{y}^2\rangle)\cos(2\phi_p) - \langle\tilde{x}\tilde{y}\rangle\sin(2\phi_p),$$

$$R_o^2 = \frac{1}{2}(\langle\tilde{x}^2\rangle + \langle\tilde{y}^2\rangle) + \frac{1}{2}(\langle\tilde{x}^2\rangle - \langle\tilde{y}^2\rangle)\cos(2\phi_p) + \langle\tilde{x}\tilde{y}\rangle\sin(2\phi_p) - 2\beta_\perp(\langle\tilde{t}\tilde{x}\rangle\cos\phi_p + \langle\tilde{t}\tilde{y}\rangle\sin\phi_p) + \beta_\perp^2\langle\tilde{t}^2\rangle,$$

$$R_{os}^2 = \langle\tilde{x}\tilde{y}\rangle\cos(2\phi_p) - \frac{1}{2}(\langle\tilde{x}^2\rangle - \langle\tilde{y}^2\rangle)\sin(2\phi_p) + \beta_\perp(\langle\tilde{t}\tilde{x}\rangle\sin\phi_p - \langle\tilde{t}\tilde{y}\rangle\cos\phi_p),$$

$$R_l^2 = \langle\tilde{z}^2\rangle - 2\beta_l\langle\tilde{t}\tilde{z}\rangle + \beta_l^2\langle\tilde{t}^2\rangle, \tag{22}$$

where

$$\langle f(x)\rangle(K) \equiv \frac{\int d^4x f(x)S(x,K)}{\int d^4x S(x,K)},$$

$$\tilde{x}^\mu \equiv x^\mu - \langle x^\mu\rangle(K). \tag{23}$$

We restrict our attention to correlations calculated in the LCMS, in which $Y=\beta_l=0$. In this case the last equation of Eqs. (22) simplifies to

$$R_l^2 = \langle\tilde{z}^2\rangle. \tag{24}$$

In the notation of Sec. II D and further defining

$$\overline{\{B\}_{j,k}} \equiv \frac{\{B\}_{j,k}}{\{1\}_{0,0}}, \tag{25}$$

the space-time correlations of interest are

$$\langle \tilde{x}^2 \rangle = \overline{\{x^2\}_{0,0}} - \overline{\{x\}_{0,0}}^2,$$

$$\langle \tilde{y}^2 \rangle = \overline{\{y^2\}_{0,0}} - \overline{\{y\}_{0,0}}^2,$$

$$\langle \tilde{x}\tilde{y} \rangle = \overline{\{xy\}_{0,0}} - \overline{\{x\}_{0,0}}\ \overline{\{y\}_{0,0}},$$

$$\langle \tilde{x}\tilde{t} \rangle = \frac{\Delta\tau^2 + \tau_0^2}{\tau_0}\left(\overline{\{x\}_{0,1}} - \overline{\{x\}_{0,0}}\ \overline{\{1\}_{0,1}}\right),$$

$$\langle \tilde{y}\tilde{t} \rangle = \frac{\Delta\tau^2 + \tau_0^2}{\tau_0}\left(\overline{\{y\}_{0,1}} - \overline{\{y\}_{0,0}}\ \overline{\{1\}_{0,1}}\right),$$

$$\langle \tilde{t}^2 \rangle = (3\Delta\tau^2 + \tau_0^2)\overline{\{1\}_{0,2}} - \left(\frac{\Delta\tau^2 + \tau_0^2}{\tau_0}\right)^2 \overline{\{1\}_{0,1}}^2,$$

$$\langle \tilde{z}^2 \rangle = (3\Delta\tau^2 + \tau_0^2)\overline{\{1\}_{2,0}}. \tag{26}$$

We note that all quantities with space-time dimensions are explicitly shown in Eqs. (26) and in particular, all dependence on the time scale parameters τ_0 and $\Delta\tau$.

The proper time of freeze-out is often estimated (e.g., [59]) by fitting the m_T dependence of the measured R_l radius to a formula motivated by Sinyukov and collaborators [43,60], and subsequently improved upon by others [44,61]. They assumed boost-invariant longitudinal flow, but vanishing transverse flow ($\rho=0\rightarrow\beta=m_T/T$) and instantaneous freeze-out in proper time (i.e., $\Delta\tau=0$); they also simplified the formalism by using Boltzmann statistics [i.e., using only the first term in the summation in Eq. (8)]. In this case, we find, in agreement with Refs. [44,61],

$$R_l^2(m_T) = \tau_0^2 \frac{T}{m_T}\frac{\mathrm{K}_2(m_T/T)}{\mathrm{K}_1(m_T/T)}. \tag{27}$$

We note that the last term, which represents a correction to the original Sinyukov formula [43,60], approaches unity for $m_T/T\rightarrow\infty$ but remains sizable ($\sim$1.5) for $m_T/T\sim 2$.

In general, the emission "homogeneity region" [62] [characterized by the correlation coefficients of Eq. (26)] and the HBT radii of Eq. (22) depend on the pair momentum [6,39]. For a boost-invariant system, this corresponds to dependences on p_T and ϕ_p. Figure 18 shows projections onto the transverse (x-y) plane of the emission regions for pions with $p_T=0.3$ GeV/c and $\phi_p=0°$, 135°, for an anisotropic source with strong transverse flow. The flow generates strong space-momentum correlations, so that particles with higher p_T tend to be emitted from the edge of the source, with $\phi_p\approx\phi_s$. Together with the finite extent of the overall source, this implies that, spatially, the emission region is often wider in the direction perpendicular to the particle motion (indicated by the arrows) than along the motion; this can have strong implications, e.g., for the difference between R_o^2 and R_s^2.

While the blast-wave parametrization provides direct access to the homogeneity region, the radii extracted from two-

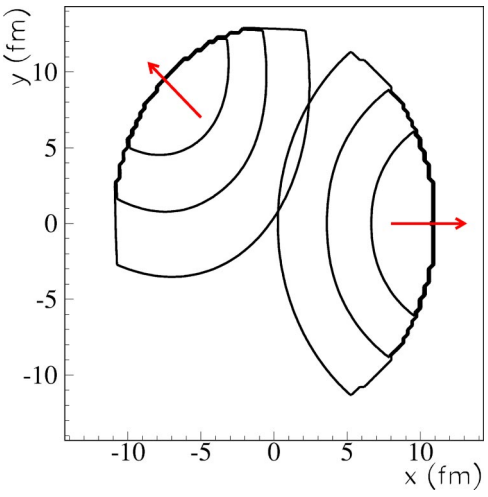

FIG. 18. (Color online) Emission probability contours, plotted on a linear scale, indicate emission zones for pions with $p_T=0.3$ GeV/c at $\phi_p=0°$ and $\phi_p=135°$ (indicated by arrows), from a blast-wave source with "nonround" default parameters listed in Table I.

pion interferometry are compared to second-order moments calculated as shown in Eqs. (26). Such comparison is strictly correct only if the homogeneity regions are Gaussian distributions. Figure 19 shows an example of spatial distributions along the three Cartesian directions for pions with two different momenta $\vec{p}=(0.25\ \mathrm{GeV}/c,0,0)$ and $\vec{p}=(0.5\ \mathrm{GeV}/c,0,0)$; in this case, the x,y and z directions correspond to "out," "side," and "long," respectively The z distribution is nearly Gaussian; the difference between the σ extracted from a Gaussian fit and the second-order moment is on the order of a few percent. On the other hand, the x and y distributions are clearly not Gaussian. To estimate the level of distortion introduced by the non-Gaussian shape, we compare the second-order moments with the Gaussian σ extracted by fitting the peak of the spatial distributions. Indeed, it has been shown in [63] that calculating correlation function from models and fitting them as experimental data yields

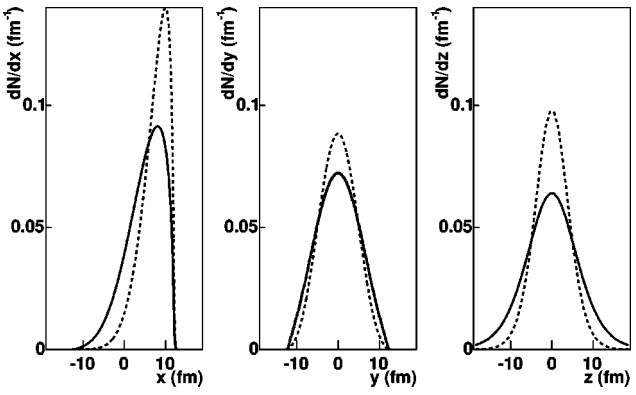

FIG. 19. Distribution of the pion spatial distribution in the direction x (left), y (middle), and z (right). Solid line: pion momentum $p_x=0.25$ GeV/c and $p_y=0$. Dashed line: pion momentum $p_x=0.5$ GeV/c and $p_y=0$. Round source parameters of Table I were used, with the exception of a_s, which was set to 0.01.

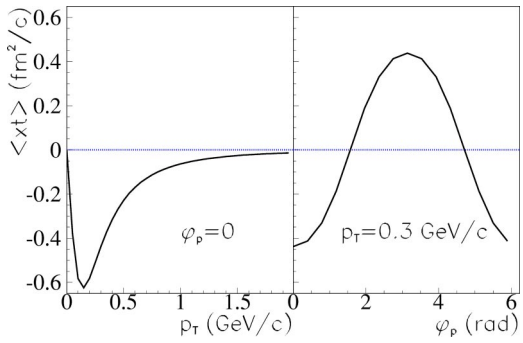

FIG. 20. (Color online) Space-time correlation $\langle \tilde{x}\tilde{t} \rangle$ as a function of p_T for $\phi_p=0$ (left panel) and as a function of ϕ_p for $p_T=0.3$ GeV/c. "Nonround" source parameters of Table I were used.

radii that are close to the Gaussian σ extracted by fitting the peak of the spatial distributons. In both the x and y directions, we find that the Gaussian σ is systematically larger than the second-order moments by up to 20% (depending on the fit range) for pions at $p_T=0.25$ GeV/c. This discrepancy diminishes when increasing the transverse momentum or the particle mass. E.g., it is on the order of 10% for pions at $p_T=0.5$ GeV/c or for kaons at $p_T=0.25$ GeV/c. Thus, comparing second-order moments with the radii extracted from two-pion correlation functions may involve significant systematic errors at low transverse mass. This issue may be overcome by calculating correlation functions from the blast-wave space-time distributions or by relying on an imaging method to extract space-time distributions from the data [64]. Applying these methods is beyond the scope of this paper and we will thus carry on keeping in mind that systematic errors are associated with comparing HBT radii with second-order moment at low transverse momentum.

On the other hand, resonance decay may introduce a core-halo pattern in the distribution of particle space-time emission points [65]. Indeed, some resonances decay sufficiently far away from the bulk of the system that their decay products emerge beyond the main homogeneity region. Such particles form a halo around the core of the source. However, to affect the extracted radii, the resonance lifetime needs to be short enough for the correlation to take place at a relative momentum accessible to the experiment. This lifetime is typically between 10 and 100 fm. The effect of resonance feed-down on radii measured by two-pion interferometry has been studied within an early version of the blast-wave parametrization [66]. It was found that the ω meson leads to a halo effect, its $c\tau$ being 23.4 fm. The other resonances have lifetimes that are either too short (e.g., ρ, Δ) or too long (e.g., η, K_s^0). At RHIC energy, thermal models [67] show that about 10% of the pions come from ω, which means that this effect should be rather small. The effect of the very long-lived ($c\tau > 100$ fm) resonances is usually assumed to reduce the so-called λ parameter [68], which we do not discuss here.

Also important are temporal effects, including space-time correlations. The average x-t correlation, quantified by $\langle \tilde{x}\tilde{t} \rangle$, for the same anisotropic source, is plotted in Fig. 20, as a function of p_T and ϕ_p. In the left panel, $\phi_p=0°$, and thus x is the "out" direction. We first note that the correlation is negative, tending to *increase* R_o^2 for finite $\beta_\perp$ [see Eq. (22)]; large and negative "out"-t correlations at freeze-out in some hydrodynamical models [69] have been a significant component of predicted large R_o^2/R_s^2 ratios. As required by symmetry [55], $\langle \tilde{x}\tilde{t} \rangle$ displays an odd-order cosine dependence on ϕ_p; clearly the first-order component dominates here, as shown in the right panel of Fig. 20. This $\cos(\phi_p)$ dependence is driven mostly by the $\cos(\phi_s)$ dependence of the x coordinate, coupled with the radial flow which tends to make $\phi_s \approx \phi_p$ (cf. Fig. 18). However, we also note from the figure that the *scale* of these correlations is $\lesssim 1$ fm$^2/c$, which, as we shall see, is much smaller than the typical scale of R_o^2; hence, space-time correlations do not dominate in the blast wave.

More important are the correlation coefficients $\langle \tilde{x}\tilde{y} \rangle$, $\langle \tilde{x}^2 \rangle$, and $\langle \tilde{y}^2 \rangle$ and their p dependence. $\langle \tilde{x}\tilde{y} \rangle$ quantifies the transverse "tilt" of the emission zone with respect to the reaction plane. As required by symmetry [55], this tilt vanishes at $\phi_p=0$, while, in the present case with $R_y > R_x$, it is positive for $\phi_p=135°$ (see Fig. 18). That $\langle \tilde{x}^2 \rangle$ and $\langle \tilde{y}^2 \rangle$ also depend on ϕ_p is likewise clear from Fig. 18. As we shall see, the ϕ_p dependence of $\langle \tilde{x}\tilde{y} \rangle$, $\langle \tilde{x}^2 \rangle$, and $\langle \tilde{y}^2 \rangle$, combined with the explicit ϕ_p dependences in Eq. (22), drive the oscillations in HBT radii which we will study.

At this point, it is worthwhile to mention that the emission zone ("homogeneity region") and the correlation coefficients $(\langle \tilde{x}^2 \rangle, \langle \tilde{y}^2 \rangle, \langle \tilde{x}\tilde{y} \rangle, \langle \tilde{x}\tilde{t} \rangle, \langle \tilde{y}\tilde{t} \rangle)$ will vary with ϕ_p also for an azimuthally *isotropic* source ($R_x=R_y, \rho_2=0$). However, of course, the measured HBT radii will be ϕ_p independent. This arises due to the cancellation and combination of terms in Eqs. (22). For R_s^2, the first term becomes ϕ_p independent, and the second and third terms *combined* are ϕ_p independent $[(\langle \tilde{x}^2 \rangle - \langle \tilde{y}^2 \rangle) \propto \cos(2\phi_p)$ and $\langle \tilde{x}\tilde{y} \rangle \propto \sin(2\phi_p)]$. For R_o^2, the story is the same for the first three terms, while the fourth term becomes ϕ_p independent as $\langle \tilde{x}\tilde{t} \rangle \propto \cos(\phi_p)$ and $\langle \tilde{y}\tilde{t} \rangle \propto \sin(\phi_p)$. Meanwhile, for R_{os}^2, the first and second terms cancel each other, as do the two components of the third term; hence $R_{os}^2=0$ for azimuthally symmetric sources. We mention these points here because several of the *exact* cancellations and combinations which hold for an *isotropic* source continue to hold *approximately* even when the geometry or flow field is anisotropic.

We turn now to a detailed study of the observable HBT radius parameters and the effects of varying blast-wave parameters. For a boost-invariant system, the symmetry-allowed ϕ_p oscillations of the (squared) HBT radii are [55]

$$
\begin{aligned}
R_s^2(p_T,\phi_p) &= R_{s,0}^2(p_T) + 2\Sigma_{n=2,4,6,\ldots} R_{s,n}^2(p_T)\cos(n\phi_p),\\
R_o^2(p_T,\phi_p) &= R_{o,0}^2(p_T) + 2\Sigma_{n=2,4,6,\ldots} R_{o,n}^2(p_T)\cos(n\phi_p),\\
R_{os}^2(p_T,\phi_p) &= 2\Sigma_{n=2,4,6,\ldots} R_{os,n}^2(p_T)\sin(n\phi_p),\\
R_l^2(p_T,\phi_p) &= R_{l,0}^2(p_T) + 2\Sigma_{n=2,4,6,\ldots} R_{l,n}^2(p_T)\cos(n\phi_p),
\end{aligned}
\tag{28}
$$

where the HBT radii Fourier coefficients $R_{\mu,n}^2$ ($\mu = o, s, os, l$ and $n=0, 2, 4, \ldots$) are ϕ_p independent.

Figure 21 shows the p_T and ϕ_p dependence of HBT radii calculated for a blast-wave source with a slightly anisotropic

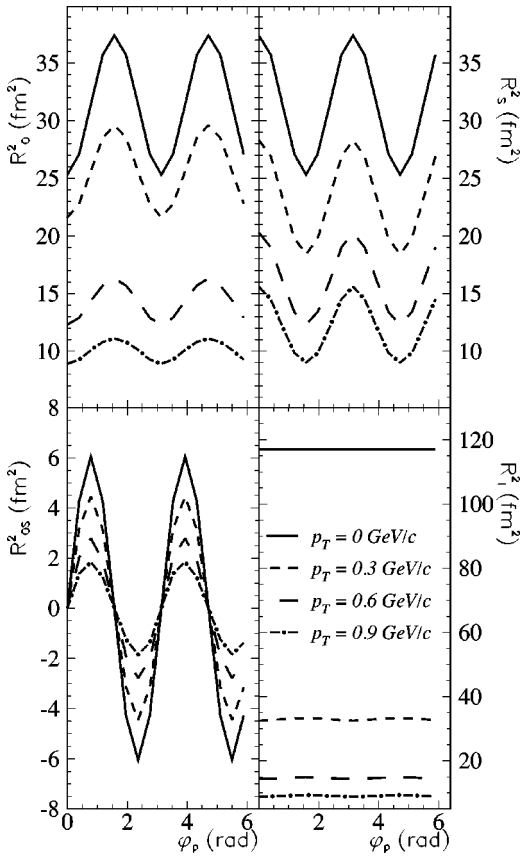

FIG. 21. Squared HBT radius parameters calculated with Eqs. (26) and (22) from a blast-wave source with the "nonround" default parameters of Table I. Squared radii for various cuts in p_T are plotted versus ϕ_p, the emission angle with respect to the event plane.

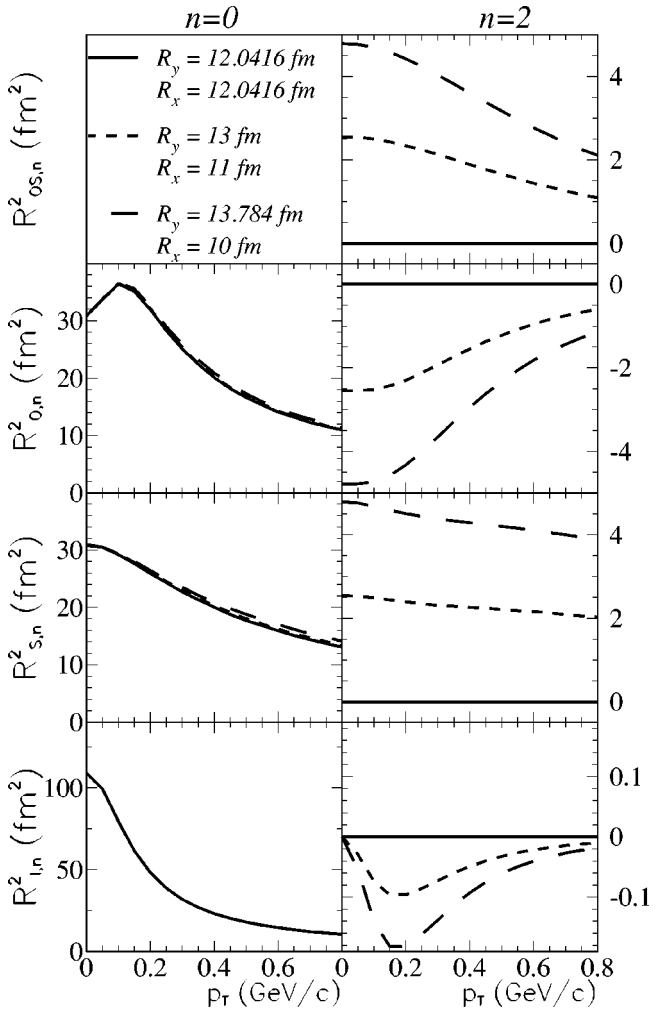

FIG. 22. Fourier coefficients of the ϕ_p dependence of the squared HBT radii, as calculated by Eq. (29). Zeroth- and second-order Fourier coefficients are plotted in the left and right panels, respectively. The transverse shape of the source (i.e., R_y/R_x) was varied, while $R_y^2+R_x^2$ was held fixed. "Round" source values from Table I are used for the other parameters.

flow field and shape. In addition to an overall decrease in the average value of the HBT radii with increasing p_T, we observe significant oscillations in the transverse radii R_o^2, R_s^2, and R_{os}^2 and smaller oscillations in R_l^2.

The Fourier coefficients may be calculated as

$$R^2_{\mu,n}(p_T) = \begin{cases} \langle R^2_\mu(p_T,\phi_p)\cos(n\phi_p)\rangle & (\mu = o,s,l), \\ \langle R^2_\mu(p_T,\phi_p)\sin(n\phi_p)\rangle & (\mu = os). \end{cases} \tag{29}$$

In the present model, we find that oscillation amplitudes above second order are very small in all cases considered ($|R^2_{\mu,4}/R^2_{\mu,2}| \lesssim 0.01$). Therefore, the ϕ_p dependence of the HBT radii at a given p_T is essentially encapsulated in seven numbers: the zeroth- and second-order Fourier coefficients of R_o^2, R_s^2, and R_l^2 and the second-order Fourier coefficient of R_{os}^2. We henceforth explore the evolution of the p_T dependence of these seven numbers, as model parameters are varied.

Figure 22 shows the Fourier coefficients for $n=0$, 2, corresponding to a blast-wave source with $T=0.1$ GeV, an isotropic flow field ($\rho_0=0.9, \rho_2=0$), a box profile ($a_s=0$), and time parameters $\tau_0=9$ fm/c, $\Delta\tau=2$ fm/c. Here, the average transverse size of the source ($R_x^2+R_y^2$) was held fixed, while the shape (R_y/R_x) was varied.

The zeroth-order Fourier coefficients (corresponding to the radii R_o, R_s, and R_l usually measured by experimentalists) are sensitive only to the average scale, not the shape, of the source. The average values of the transverse radii $R_{o,0}^2$ and $R_{s,0}^2$ fall with increasing p_T due to radial flow [6,44] (cf. Fig. 31). At intermediate values of p_T, $R_{o,0}^2 > R_{s,0}^2$ due to finite time scale effects (cf. Figs. 29 and 30), but at high p_T, $R_{o,0}^2 < R_{s,0}^2$ (i.e., $R_o/R_s < 1$), in qualitative agreement with experimental data [59,70]. The boost-invariant longitudinal flow produces the strong decrease of $R_{l,0}^2$ with p_T [6,43,44,60,61].

Richer detail is seen in the *oscillations* of the HBT radii, quantified by Fourier coefficients $R_{\mu,2}^2$ in the right-hand panels of Fig. 22. Here, the elliptical shape of the source is explicitly clear. The signs of the second-order Fourier coefficients of the transverse radii directly reflect the out-of-plane-extended source geometry when $R_y > R_x$. $R_{os,2}^2$ has a similar geometric interpretation, in terms of the ϕ_p evolution of the "tilt" of the homogeneity region [23]. The relatively

small oscillations in R_l^2 arise not directly from geometry, but instead from transverse flow gradients, which slightly reduce R_l^2 [44]. In the present example, the transverse flow increases linearly from 0 (at the center) to $\rho_0=0.9$ (at the edge of the source), independent of boost angle ϕ_b. However, when $R_y>R_x$, the flow *gradient* is larger for source elements boosted in plane, leading to a slightly greater reduction of R_l^2 when $\phi_p=0$; hence, $R_{l,2}^2<0$.

Finally, we recall that the flow field is isotropic ($\rho_2=0$) and so all ϕ_p dependence arises from geometry here. Thus, if the values of R_y and R_x are interchanged (corresponding to *in-plane*-extended sources), $R_{\mu,0}^2$ would remain unchanged, and $R_{\mu,2}^2$ would simply change in sign in Fig. 22.

As discussed above, transverse flow-induced space-momentum correlations tend to decrease homogeneity lengths as p_T increases. When combined with other effects (e.g., temporal effects), nontrivial p_T dependences of the HBT radii result. The p_T dependences of the ϕ_p-averaged values $R_{\mu,0}^2$ have been discussed extensively [6,44]. Meanwhile, the p_T dependences of the oscillation amplitudes ($R_{\mu,2}^2$) shown in the right panels of Fig. 22 have not been explored previously and may be nontrivial in principle.

It was suggested [71] that the p_T dependence of $|R_{\mu,2}^2|$ might be driven largely by the same effects which generate the p_T dependence of $R_{\mu,0}^2$, and hence the most efficient and direct way to study the source is to plot $R_{\mu,0}^2$, which encode scale information, and then the *ratio* of second- to zeroth-order Fourier coefficients, which would encode geometric and dynamic anisotropy. This is an excellent suggestion, though consideration must be given to the appropriate scaling. First, we consider the transverse radii R_o^2, R_s^2, and R_{os}^2. The radii R_o^2 and R_{os}^2 encode both transverse geometry *and* temporal information. As discussed above, space-time (e.g., x-t) correlations are small in magnitude and, furthermore, affect the HBT radii in combinations which tend to cancel any ϕ_p dependence. Therefore, we expect $R_{o,0}^2$, $R_{s,0}^2$, $R_{s,2}^2$, $R_{o,2}^2$, and $R_{os,2}^2$ to contain geometric contributions, while temporal contributions are significant only for $R_{o,0}^2$. In this case, the appropriate ratios to study are $R_{o,2}^2/R_{s,0}^2$, $R_{s,2}^2/R_{s,0}^2$, and $R_{os,2}^2/R_{s,0}^2$. Indeed, we find numerically that these are the ratios least affected by the overall scale of the homogeneity region, which varies both with p_T and with model parameter. The oscillation strength $R_{l,2}^2$ of the longitudinal radius, on the other hand, is entirely due to implicit ϕ_p dependences driven by space-momentum correlations; these same correlations affect $R_{l,0}^2$. Hence, the appropriate ratio to study in this case is $R_{l,2}^2/R_{l,0}^2$.

In Fig. 23 we show these ratios for the same sources as were plotted in Fig. 22. The p_T dependence of the ratios is significantly less than that of the oscillation strengths $R_{\mu,2}^2$, as anticipated, due to the fact that the latter is driven largely by space-momentum correlations reducing the spatial scale of the homogeneity region.

Going further, we may recall that in the special case of vanishing space-momentum correlations ($\rho=0$ or $T=\infty$), the transvserse radii oscillate with identical strengths ($R_{os,2}^2=R_{s,2}^2=-R_{o,2}^2$), and the in-plane and out-of-plane extents of the source may be directly extracted [39,55–57], as the "whole source" is viewed from every angle. In that special case, independent of p_T,

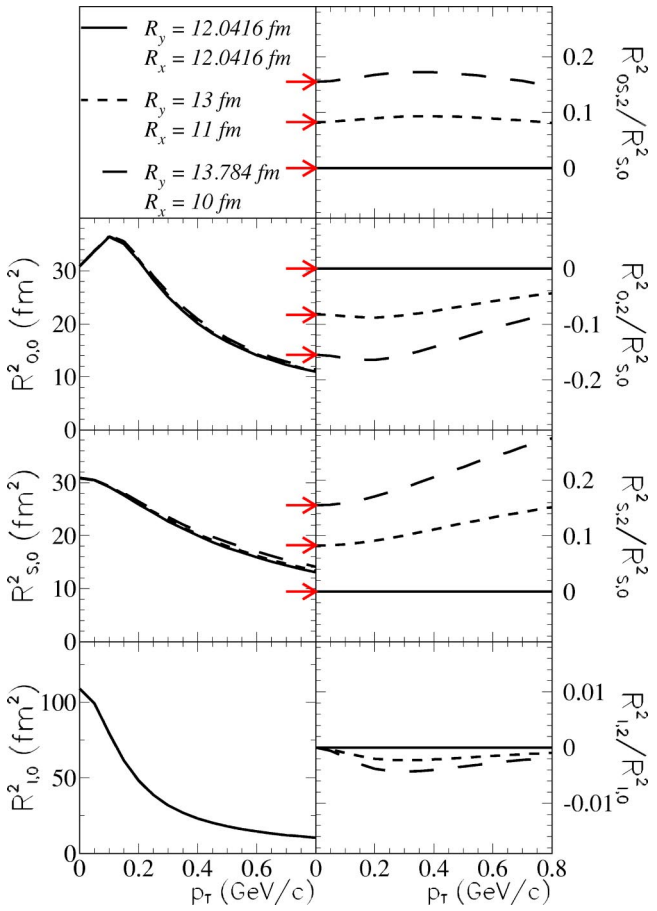

FIG. 23. (Color online) Identical data as in Fig. 22, except the right panels show ratios of second- and zeroth-order Fourier coefficients of the ϕ_p dependence of the squared HBT radii. Arrows indicate values calculated from Eq. (32); see text for details.

$$R_{s,0}^2=\frac{1}{2}(\langle\tilde{y}^2\rangle+\langle\tilde{x}^2\rangle)=\frac{1}{8}(R_y^2+R_x^2), \tag{30}$$

$$R_{os,2}^2=R_{s,2}^2=-R_{o,2}^2=\frac{1}{4}(\langle\tilde{y}^2\rangle-\langle\tilde{x}^2\rangle)=\frac{1}{16}(R_y^2-R_x^2), \tag{31}$$

so that

$$\frac{R_{os,2}^2}{R_{s,0}^2}=\frac{R_{s,2}^2}{R_{s,0}^2}=-\frac{R_{o,2}^2}{R_{s,0}^2}=\frac{1}{2}\frac{R_y^2-R_x^2}{R_y^2+R_x^2}\equiv\frac{\epsilon}{2}. \tag{32}$$

In the presence of flow, however, HBT radii measured at momentum $\vec{p}$ reflect homogeneity lengths which in principle may vary nontrivially both with p_T and ϕ_p. While we find that nonvanishing flow violates the p_T independence of $R_{s,0}^2$, $R_{o,2}^2$, $R_{s,2}^2$, and $R_{os,2}^2$ [and thus Eqs. (30) and (31)], Eq. (32) remains remarkably robust. As seen in the next several figures, the ratios $R_{o,2}^2/R_{s,0}^2$, $R_{s,2}^2/R_{s,0}^2$, and $R_{os,2}^2/R_{s,0}^2$, largely independent of p_T, provide an estimate of the source ellipticity ϵ. Arrows to the left of the panels for $R_{o,2}^2/R_{s,0}^2$, $R_{s,2}^2/R_{s,0}^2$, and $R_{os,2}^2/R_{s,0}^2$ in Figs. 23–34 indicate $\epsilon/2$ for the sources used.

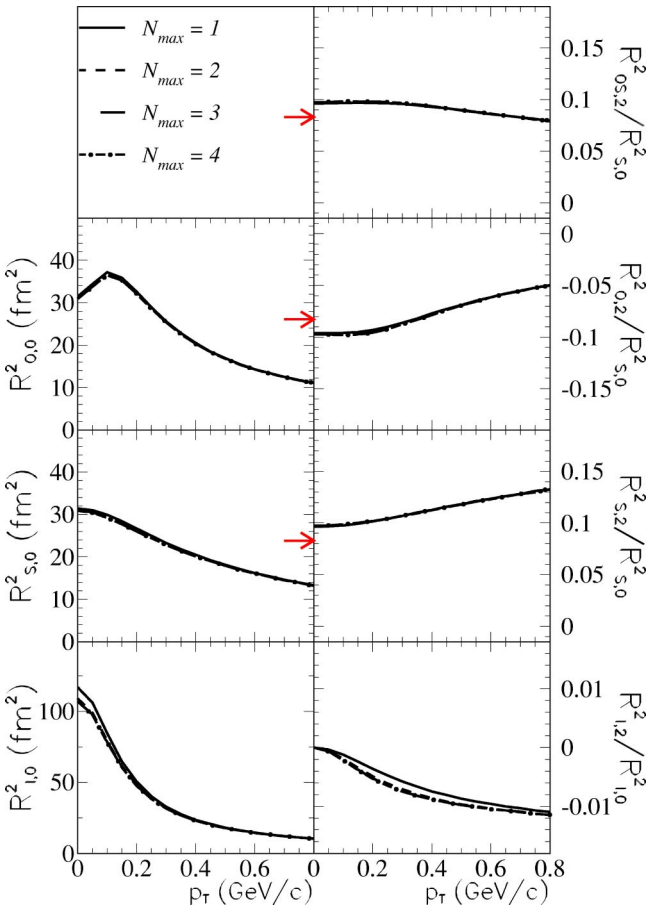

FIG. 24. (Color online) Fourier coefficients of the ϕ_p dependence of the squared HBT radii, as calculated by Eq. (29) using several values of N, the maximum value of n taken in the summation of Eq. (8). Values of the blast-wave parameters are for a "nonround" source, as listed in Table I. Arrows indicate values calculated from Eq. (32). See text for details.

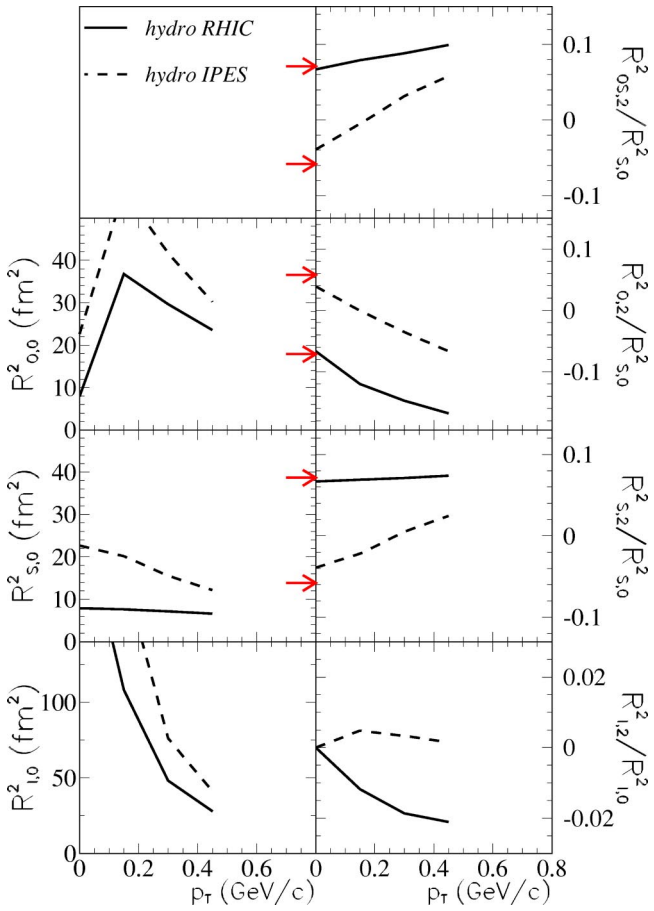

FIG. 25. (Color online) Fourier coefficients of the ϕ_p dependence of the squared HBT radii, as calculated by Eq. (29). The data are not from blast-wave calculations, but from the hydrodynamic calculations of Heinz and Kolb [23], for two different equations of state and initial conditions. Arrows indicate values calculated from Eq. (32) and extracted values of freeze-out edge radii; see text for details.

Now that we have established the quantities to be examined in this section, we briefly check the importance of using quantum, rather than classical, statistics in the source function of Eq. (8). Setting the parameter values to correspond to the "nonround" source of Table I, we plot in Fig. 24 the Fourier coefficients corresponding to different values of N, where the summation in Eq. (8) [and Eqs. (12) and (18)] is over $n=1,\ldots,N$. Once again, we find a small difference between the curves for $N=1$ and $N>1$, while inclusion of higher terms in the summation has essentially no effect. Blast-wave calculations in this section correspond to $N=2$.

Recently, Heinz and Kolb, in a hydrodynamic model, calculated HBT radii as a function of ϕ_p for noncentral collisions [23]. They used two different equations of state and initial conditions: one ("RHIC") is appropriate for soft physics at RHIC energies and has successfully reproduced momentum-space observables [9]; the other ("IPES") assumes extremely high initial energy densities, perhaps appropriate for collisions at LHC energies.

It is worthwhile to point out that even the "RHIC" hydrodynamic calculations fail to reproduce azimuthally integrated HBT data [9]; here, however, we simply investigate the connection between the freeze-out geometry and oscillations of the HBT radii. Both calculations result in a freeze-out configuration, integrated over p_T, which is rather sharp edged in transverse coordinate space; thus, we may extract surface radii R_x and R_y to calculate ϵ.

Figure 25 shows the same quantities as plotted in Fig. 23, but extracted from these hydrodynamic calculations. The "RHIC" source, which is geometrically extended out of plane ($R_y > R_x$, resulting in a positive ϵ), generates oscillations in the transverse radii with the same phase as out-of-plane sources in blast-wave calculations. For this source, the connection between ϵ and the radius oscillations [Eq. (32)] is most robust for $R^2_{s,2}$ and least well satisfied for $R^2_{o,2}$, an effect not observed in the blast wave. However, our blast-wave parametrization does not include explicit ϕ_p dependence of the temporal scale, which would affect $R^2_{o,2}$ and, to a lesser degree, $R^2_{os,2}$. Instead of attempting a more sophisticated parametrization, we simply note this fact and would recommend that an experimental estimation of the source deformation ϵ is probably best extracted from $R^2_{s,2}/R^2_{s,0}$, which should be unaffected by the azimuthal structure of the temporal

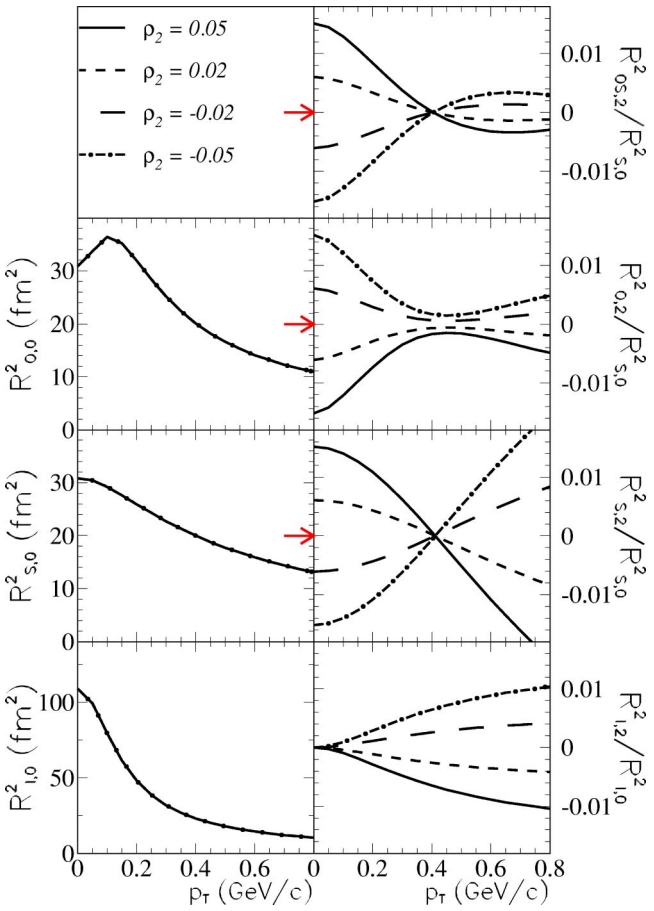

FIG. 26. (Color online) Fourier coefficients of the ϕ_p dependence of the squared HBT radii, as calculated by Eq. (29). The anisotropy of the flow field (ρ_2) is varied. Values of the other parameters are for a "round" source, as listed in Table I. Arrows indicate values calculated from Eq. (32); see text for details.

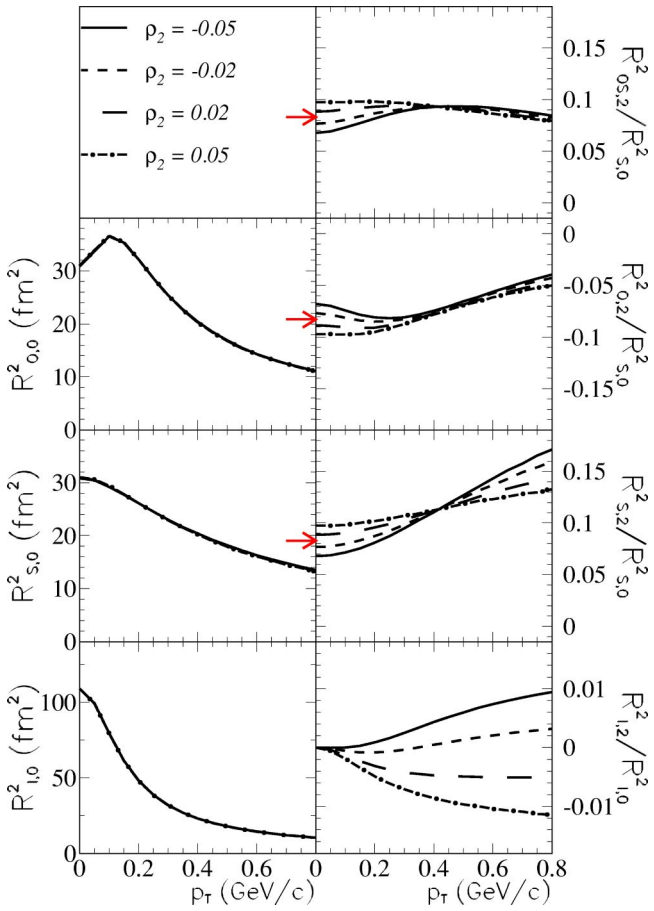

FIG. 27. (Color online) Fourier coefficients of the ϕ_p dependence of the squared HBT radii, as calculated by Eq. (29). The anisotropy of the flow field (ρ_2) is varied. Values of the other parameters are for a "nonround" source, as listed in Table I. Arrows indicate values calculated from Eq. (32); see text for details.

scale. From the study (below) of parameter variations in the blast wave, the approximation $\epsilon \approx 2R^2_{s,2}/R^2_{s,0}$ is good to ~30%, for RHIC-type sources.

Figure 25 also shows results from the "IPES" hydrodynamic calculation. Here, the freeze-out shape is extended in plane [23], but dynamical effects are so strong in this extreme case that even the sign of the transverse radius oscillations changes with p_T. The relationships in Eq. (32) work only at low p_T and, even there, only very approximately. According to this model, then, geometrical considerations dominate the HBT radius oscillations, while dynamical effects begin to dominate at much higher energies.

In Fig. 26, the source geometry is azimuthally isotropic ($R_x = R_y = 12.042$ fm), while the flow field is varied from having a stronger boost in plane ($\rho_2 > 0$) to a stronger boost out of plane ($\rho_2 < 0$). We notice again that the average HBT radius values $R^2_{\mu,0}$ are unaffected by the anisotropy. The oscillations ($R^2_{\mu,2}$) are driven by flow gradients. Naively, one would expect that all HBT radii R_o, R_s, and R_l would be smaller when the emission angle ϕ_p is in the direction of the strongest boost. For $\rho_2 = 0.05$, for example, the radii would be smaller at $\phi_p = 0$, the direction of stronger transverse boost; this would correspond to $R^2_{\mu,2} < 0$ ($\mu = o, s, l$). For $\mu = o$ and $\mu = l$, this is indeed observed, at all p_T. $R^2_{s,2}$, however, changes sign from positive at low p_T, to negative at high p_T. This behavior at low p_T is due to an effect similar to that which led to negative proton v_2 at low p_T, even when $\rho_2 > 0$. (See discussion surrounding Fig. 12.) In the present case, the particles with $p_T \approx 0$ are more likely to be emitted by source elements positioned along the y axis, due to the strong in-plane boost for source elements with large spatial coordinate x. The homogeneity region for $p_T = 0$ particles is independent of ϕ_p and has a larger extent out of plane than in plane. Thus we find the counterintuitive result that $R^2_s(\phi_p = 0) > R^2_s(\phi_p = \pi/2) \rightarrow R^2_{s,2} > 0$ at $p_T \approx 0$. We note that a similar argument holds for R^2_o, except that it leads to the conclusion that $R^2_{o,2} < 0$ at $p_T \approx 0$, and so goes in the same direction as flow-gradient effects. It is only for R^2_s that the two effects compete.

Finally, comparing the scales on the right-hand panels of Figs. 23 and 26, it is clear that, while the second-order coefficients are driven by both anisotropic geometry and flow field, a variation in geometry (R_y/R_x) has a stronger effect on $R^2_{\mu,2}$ than a variation in ρ_2, when these parameters are varied by amounts which would generate a similar effect on elliptic flow v_2 (cf. Figs. 14 and 16). Thus, measurement of both v_2

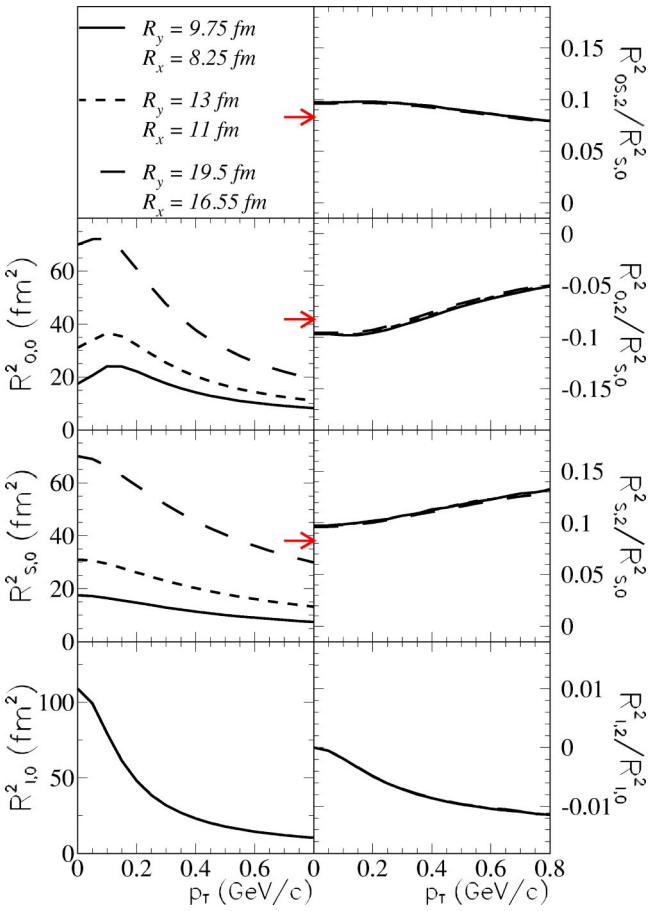

FIG. 28. (Color online) Fourier coefficients of the ϕ_p dependence of the squared HBT radii, as calculated by Eq. (29). The overall transverse scale ($\sqrt{R_y^2+R_x^2}$) is varied, while keeping $R_y/R_x=13/11$. Values of the other parameters are for a "nonround" source, as listed in Table I. Arrows indicate values calculated from Eq. (32); see text for details.

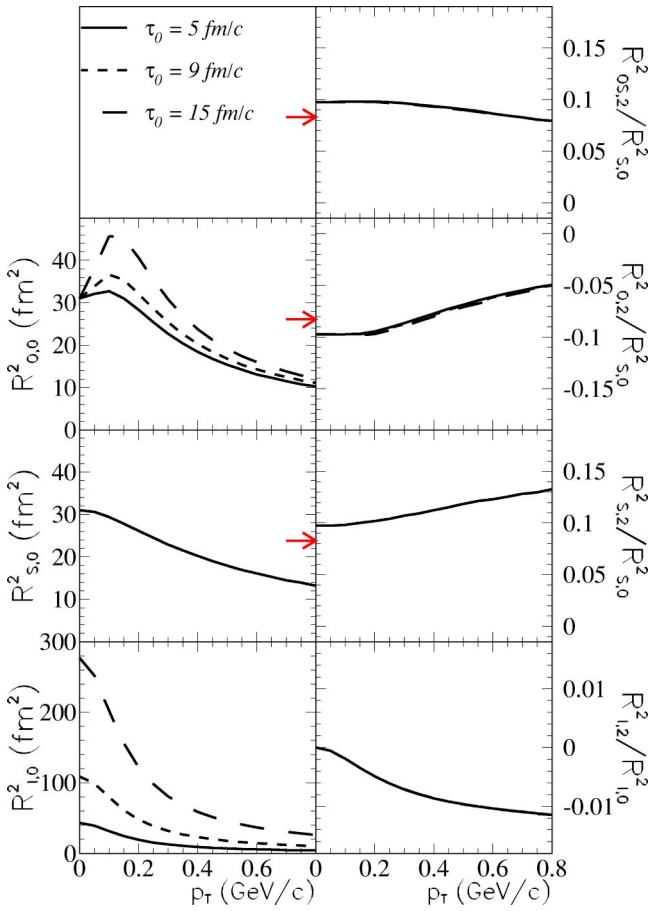

FIG. 29. (Color online) Fourier coefficients of the ϕ_p dependence of the squared HBT radii, as calculated by Eq. (29). The evolution duration τ_0 is varied. Values of the other parameters are for a "nonround" source, as listed in Table I. Arrows indicate values calculated from Eq. (32); see text for details.

and HBT radius oscillations would allow independent determination of both anisotropic flow strength ρ_2 and shape R_y/R_x.

In Fig. 27, we consider anisotropy simultaneously in both the source geometry and the flow field. The source is extended out of plane ($R_y=13$ fm and $R_x=11$ fm) and the flow anisotropy (ρ_2) varied. The zeroth-order coefficients remain unaffected by the anisotropies, while the $R^2_{\mu,2}$ reflect essentially the cumulative effects of the geometric anisotropy (shown in Fig. 23) and the flow field anisotropy (shown in Fig. 26), with no strong nonlinear coupling between them. Thus, while *in principle* anisotropic flow effects may mask or dominate geometric anisotropy [9], flow field anisotropies represent small perturbations on the dominant geometric effects in the blast wave, using "realistic" (cf. Sec. IV) parameters.

In Fig. 28 we show the effect of increasing the transverse size of the source ($\sqrt{R_y^2+R_x^2}$) while keeping the shape (R_y/R_x) and other source parameters fixed. As expected, the purely spatial transverse radius R_s^2 (average and oscillation amplitude) increases proportionally with $R_y^2+R_x^2$. The squared "outward" radius parameter R_o^2 contains both spatial components (which increase with $R_y^2+R_x^2$) and temporal components (which do not). Thus, its average value $R^2_{o,0}$ increases almost proportionally to $R_y^2+R_x^2$ at low p_T ($\beta_\perp\sim 0$) and less so at higher p_T. Due to the near cancellation of the ϕ_p dependence of temporal terms, the increase in oscillation amplitudes $R^2_{os,2}$ and $R^2_{os,2}$ is driven mainly by the spatial terms, so that $R^2_{o,2}/R^2_{s,0}$ and $R^2_{os,2}/R^2_{s,0}$ display almost no sensitivity to $R_y^2+R_x^2$ at any p_T. The longitudinal radius R_l^2 is unaffected by variation in the transverse scale.

In Figs. 29 and 30, we vary the time scale parameters τ_0 and $\Delta\tau$, respectively. All dependence of $R^2_{\mu,n}$ on these parameters comes directly through the dependence of $\langle\tilde{x}_\mu\tilde{x}_\nu\rangle$, which are listed explicitly in Eqs. (26). After an inspection of those equations, it is unsurprising that the effects of varying these parameters are similar. The space-time correlation coefficients which depend on the time scale parameters are $\langle\tilde{x}\tilde{t}\rangle$, $\langle\tilde{y}\tilde{t}\rangle$, $\langle\tilde{t}^2\rangle$, and $\langle\tilde{z}^2\rangle$. According to Eq. (22), then, $R^2_{s,0}$ and $R^2_{s,2}$ are unaffected by variations in τ_0 and $\Delta\tau$. $R_l^2=\langle\tilde{t}^2\rangle$ is directly proportional to $(3\Delta\tau^2+\tau_0^2)$, so $R^2_{l,0}$ and $R^2_{l,2}$ both scale with that quantity. Turning to the HBT radii with both spatial and temporal contributions, we again find that the ϕ_p dependence of the temporal terms is negligible, so that $R^2_{o,2}/R^2_{s,0}$ and $R^2_{os,2}/R^2_{s,0}$ are independent of the time scales,

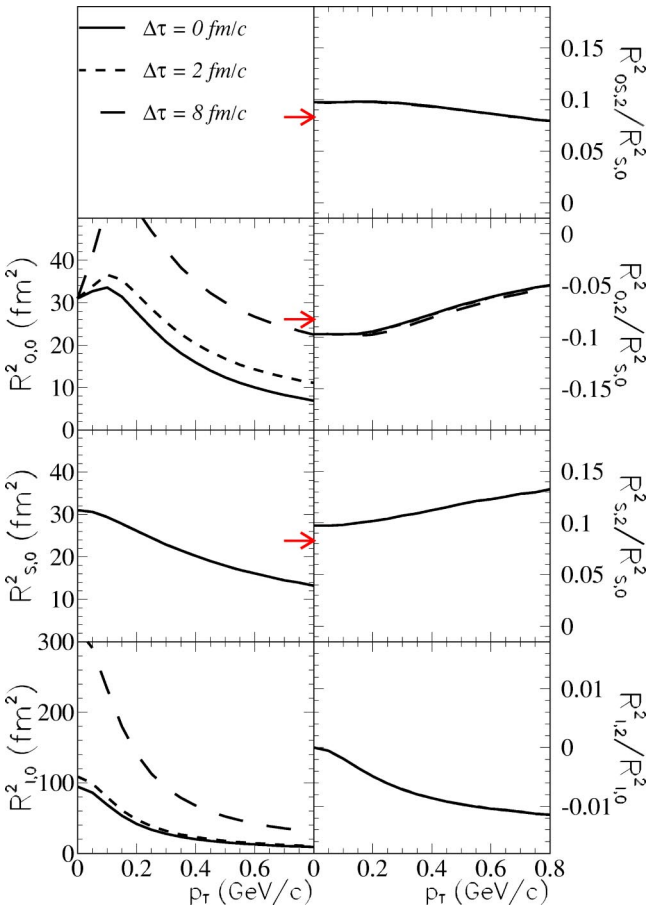

FIG. 30. (Color online) Fourier coefficients of the ϕ_p dependence of the squared HBT radii, as calculated by Eq. (29). The evolution duration $\Delta\tau$ is varied. Values of the other parameters are for a "nonround" source, as listed in Table I. Arrows indicate values calculated from Eq. (32); see text for details.

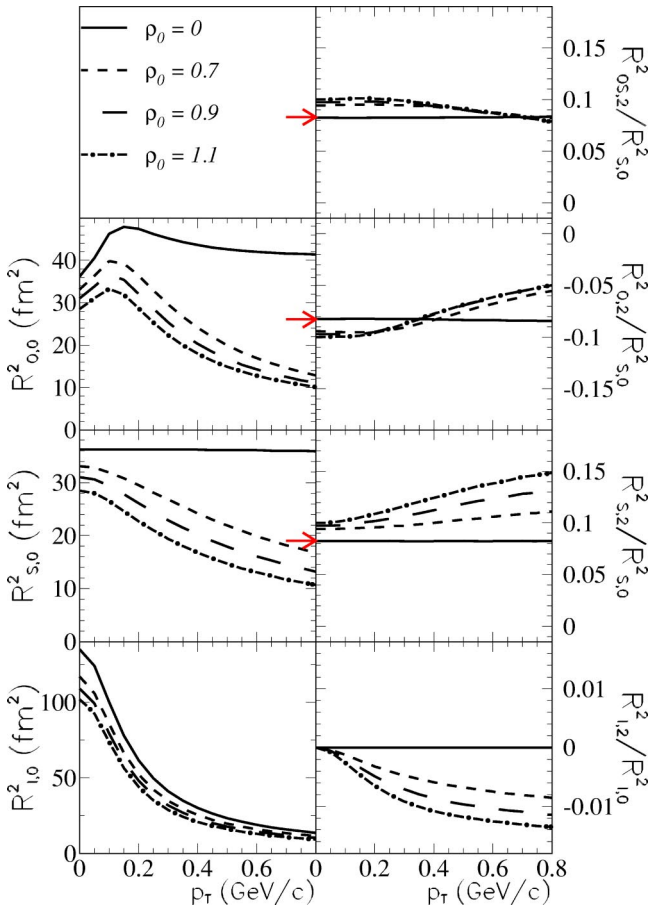

FIG. 31. (Color online) Fourier coefficients of the ϕ_p dependence of the squared HBT radii, as calculated by Eq. (29). The average radial flow magnitude ρ_0 is varied. Values of the other parameters are for a "nonround" source, as listed in Table I. Arrows indicate values calculated from Eq. (32); see text for details.

while $R^2_{o,0}$ displays the well-known [6] sensitivity to the time scale.

Thus, we find that, in the blast-wave parametrization, essentially all sensitivity to time scales comes through the ϕ_p-independent quantities $R^2_{o,0}$ and $R^2_{l,0}$. However, it is important to point out that an experimental estimate of the freeze-out geometric anisotropy, defined in Eq. (32), from measurements of the $R^2_{\mu,n}$ *would* place an additional constraint on the evolution time scale τ_0. In particular, the large initial-state anisotropy in coordinate space ($R_y > R_x$) in a noncentral collision will be reduced due to stronger flow in plane than out of plane ($\rho_2 > 0$ in the present parametrization). If the source lives for a long time (large τ_0), the system may become round ($R_y = R_x$) or even in-plane extended ($R_y < R_x$) [24]. A quantitative constraint on τ_0 from the relationship of the initial to freeze-out anisotropies, however, must be made in the context of a realistic dynamical model and is beyond the scope of the blast-wave parametrization.

In Fig. 31, the effect of variations in the ϕ-averaged ("radial") flow on the HBT radius parameters is shown. As is well known [6], stronger flow reduces the homogeneity lengths, and, indeed, almost all of the $|R^2_{\mu,n}|$ fall with increasing ρ_0. The one interesting exception is $R^2_{l,2}$; while the average scale of the longitudinal radius ($R^2_{l,0}$) decreases as the flow is increased, its ϕ_p dependence ($|R^2_{l,2}|$) *increases* (and so, then, does $|R^2_{l,2}/R^2_{l,0}|$). This is because there is no explicit ϕ_p dependence in $R^2_l = \langle \tilde{z}^2 \rangle$; any ϕ_p dependence is implicit and thus is generated by space-momentum correlations [39], which, in this model, arise solely from flow. In the no-flow limit for a boost-invariant source, $\langle \tilde{t}^2 \rangle$, $\langle \tilde{x}^2 \rangle$, $\langle \tilde{y}^2 \rangle$, and $\langle \tilde{z}^2 \rangle$ are all ϕ_p-independent constants [39,55,56].

Indeed, it is for a similar reason that $R^2_{l,2}$ vanishes for $p_T = 0$, independent of model parameter in Figs. 23–32. At $p_T = 0$, symmetry demands that none of the spatial correlation coefficients $\langle \tilde{x}_\mu \tilde{x}_\nu \rangle$ may depend on ϕ_p. Hence, only HBT radii with *explicit* ϕ_p dependence may exhibit an oscillation in that limit.

Finally, we note in Fig. 31 that the oscillation strengths $|R^2_{o,2}|$ and $|R^2_{s,2}|$ are somewhat less diminished (at low p_T), by increasing radial flow, than is $R^2_{s,0}$, which measures the overall spatial scale of the homogeneity region. Here, we offer no simple insights into the interplay between the increasing deformation of the homogeneity region and its decreasing scale, but simply note that the dependence of the scaled oscillation strengths on ρ_0 is rather small, especially at low p_T,

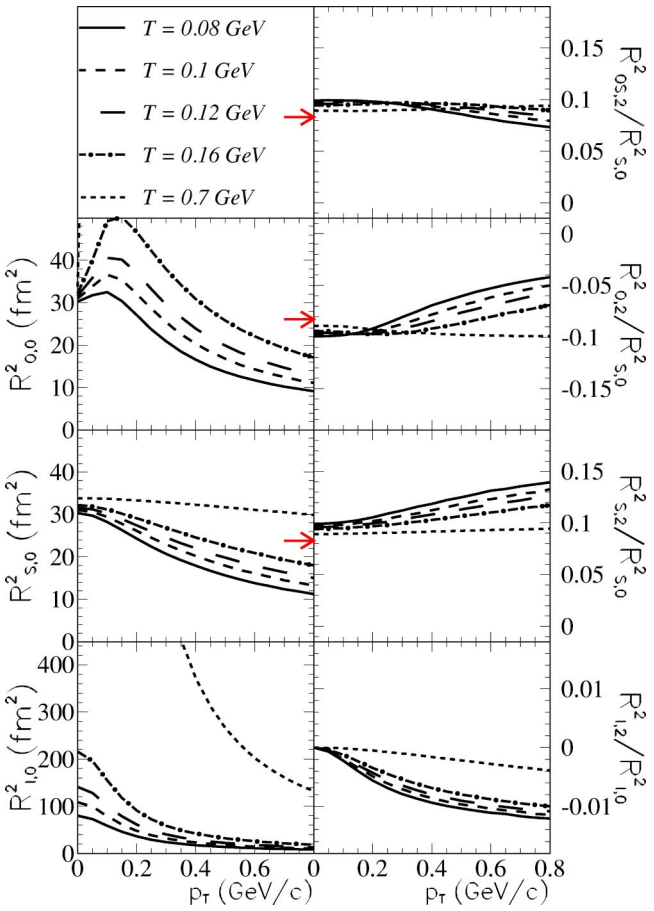

FIG. 32. (Color online) Fourier coefficients of the ϕ_p dependence of the squared HBT radii, as calculated by Eq. (29). For $T=0.7$ GeV/c, $R^2_{o,0}$ and $R^2_{l,0}$ curves partially exceed the displayed scale. Values of the other parameters are for a "nonround" source, as listed in Table I. Arrows indicate values calculated from Eq. (32); see text for details.

even for the unrealistic case of no average transverse flow ($\rho_0=0$).

Figure 32 explores the effect on HBT radii of varying the temperature parameter T. Increasing T increases "thermal smearing," reducing the flow-induced space-momentum correlations. It is well known that this leads to increased homogeneity lengths and HBT radii [35], as reflected in the left panels of the figure. In the present model, we find a small residual dependence of $R^2_{\mu,2}$ on T beyond the scaling of $R^2_{\mu,0}$ (right panels).

In the limit of very high temperature, all space-momentum correlations are eliminated, and all oscillations of HBT radii are again due to the explicit ϕ_p dependence in Eqs. (22). Then, we find that Eqs. (30)–(32) hold, independent of p_T. For the source of Fig. 32, according to Eq. (32), $|R^2_{\mu,2}/R^2_{s,0}|=0.083$. Finally, $R^2_{l,2}$ decreases with increasing T and must vanish at $T\to\infty$ when all space-momentum correlations are destroyed.

Finally, we consider the effect of a finite "skin thickness" a_s. As in the discussions surrounding Figs. 7 and 17, it is appropriate to scale the flow parameters according to $F(a_s)$ given in Eq. (20). Moreover, it is clearly appropriate to scale

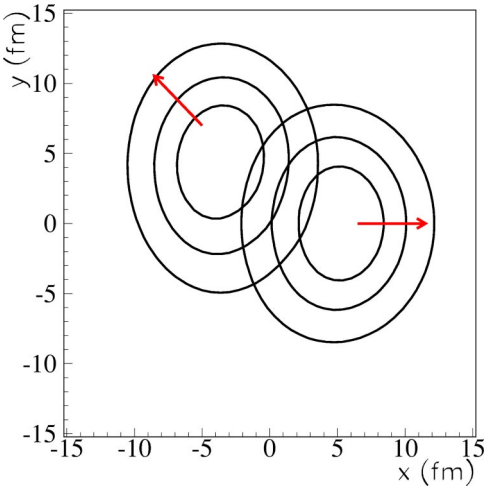

FIG. 33. (Color online) Emission probability contours, plotted on a linear scale, indicate emission zones for pions with $p_T=0.3$ GeV/c at $\phi_p=0°$ and $\phi_p=135°$ (indicated by arrows), from a blast-wave source with $a_s=0.3$. Other parameter values correspond to the "nonround" values listed in Table I.

the geometric size parameters R_y and R_x, as the overall scale of the source will increase with a_s, if these parameters remain fixed. Less clear is the exact scaling which would keep, e.g., $R^2_{s,0}$ independent of a_s, especially in the presence of finite flow. For illustrative purposes, we scale R_y and R_x also by $F(a_s)$, so that $R_y=13.0$, 12.21, and 8.84 fm, for $a_s=0$, 0.1, and 0.3, respectively; $R_y/R_x=13/11$ in all cases. This scaling keeps $\langle|r|\rangle$, as well as the flow gradient, the same in each case.

Figure 33 shows homogeneity regions projected onto the x-y plane, for a blast-wave source with $a_s=0.3$, corresponding to a pseudo-Gaussian geometrical distribution in $\tilde{r}$ (see Fig. 1). Comparing Figs. 18 and 33, we observe that the lack of a "hard cutoff" in coordinate space in the latter case leads to less reduction in the "out" direction (i.e., along the direction of motion). Thus, the important ratio $R^2_{o,0}/R^2_{s,0}$ will be larger at finite p_T, when $a_s=0.3$.

We also note that the shape and size of the homogeneity region itself depend much less on ϕ_p, when $a_s=0.3$. The homogeneity region for pions emitted to $\phi_p=135°$ is essentially a spatially translated (and unrotated) replica of that for pions emitted to $\phi_p=0°$. Since HBT correlations are insensitive to a spatial translation of the source, the situation for $a_s=0.3$ is rather similar to the situation in which no flow is present. In the no-flow case, the same homogeneity region is measured at all angles, and all oscillations of the HBT radii arise from the explicit ϕ_p dependence in Eqs. (22) [39,56]; for the source in Fig. 33, not the same region, but a (virtually) identical one, is being measured at all angles ϕ_p.

This has implications for the oscillations of the transverse radii. Focusing on the homogeneity regions for $\phi_p=135°$, we observe that while $\langle\tilde{x}\tilde{y}\rangle$ (which quantifies the "tilt" of the homogeneity region relative to the x and y axes) is greater when $a_s=0$, R^2_{os} (which quantifies the tilt of the homogeneity region relative to the "out" and "side" directions [23]) is larger for $a_s=0.3$. Therefore, we expect larger values of $R^2_{os,2}$ for larger a_s.

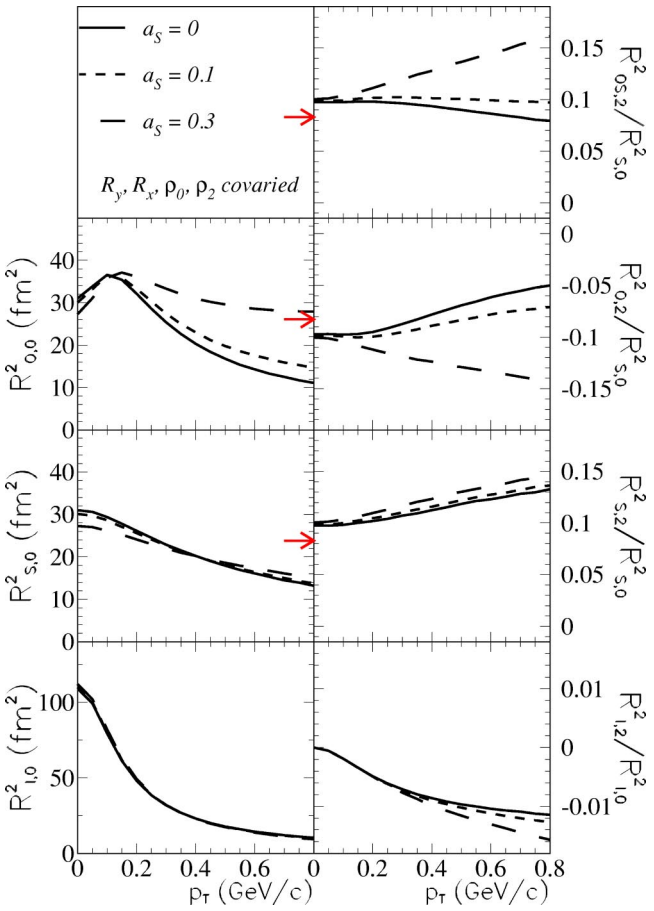

FIG. 34. (Color online) Fourier coefficients of the ϕ_p dependence of the squared HBT radii, as calculated by Eq. (29). The parameters T, τ_0, and $\Delta\tau$ are set to values listed in Table I, while the parameters ρ_0, ρ_2, R_y, and R_x are covaried with the surface diffuseness a_s; see text for details.

Figure 34 shows quantitatively the effects on the HBT radii, when a_s is varied. As intended by the scaling of flow and size parameters with $F(a_s)$, $R^2_{s,0}$ remains approximately invariant when the parameters are covaried. As discussed above, $R^2_{o,0}/R^2_{s,0}$ grows with a_s at finite p_T, as do the magnitudes of the oscillation strengths $|R^2_{o,2}/R^2_{s,0}|$, $|R^2_{os,2}/R^2_{s,0}|$, and $|R^2_{s,2}/R^2_{s,0}|$. The average value of R^2_l remains roughly constant, while its oscillation amplitude increases slightly with a_s, due to x-z and y-z correlations.

D. Nonidentical particle correlations

Final-state interactions between pairs of nonidentical particles (e.g., K-π) are sensitive to the space-time structure (size, shape, emission duration) of the emitting source, analogously to HBT correlations between identical particles. Most importantly, the authors of Refs. [53,72,73] show that studying correlations between nonidentical particles reveals new information about the average relative space-time separation between the emission of the two particles, in the rest frame of the pair. This unique information may be extremely valuable to determine the interplay between partonic and hadronic effects. For example, the lower hadronic cross section of kaons compared to pions may cause them to be emitted earlier and closer to the center of the source than pions. However, if most of the system evolution takes place at the parton level, the space-time emission pattern of pions and kaons would be similar. This example is far from unique as the same kind of argument can be made for protons recalling that the pion-proton hadronic cross section is very large or, conversely, to Ξ and Ω whose hadronic cross section is expected to be small. Furthermore, in terms of temporal effects, strangeness distillation [74,75] or other unique physics may cause some particles to be emitted later than others. Preliminary analyses of the $\pi^{\pm}-K^{\pm}$, $\pi^{\pm}-p^{\pm}$, and $K^{\pm}-p^{\pm}$ correlation functions have been reported by the STAR Collaboration in Au-Au collisions at $\sqrt{s_{NN}}=130$ GeV and 200 GeV [76,77]. These analyses show that pions, kaons, and protons are not emitted at the same average space-time point.

The blast-wave parametrization implicitly assumes that the particle freeze-out conditions (temperature, flow profile, freeze-out time, and position) are the same for all particle species. However, as shown earlier, the transverse momentum spectra and elliptic flow or different particle species do not look alike. Indeed, the relative contribution of the random emission (quantified by temperature) and collective expansion depends directly on particle masses. The same phenomenon is likely to affect the particle freeze-out space-time emission distribution. In this section, we will show that collective flow effects implicit in the blast-wave parametrization induce a shift between the average freeze-out space-time point of different particle species. We will then study how changing the blast-wave parameters affects these average freeze-out separations.

1. Nonidentical particle and blast-wave formalism

Two particles interact when they are close to each other in phase space in the local pair rest frame. Thus, particle pairs may be correlated when their relative momentum in the pair rest frame is small. For particles with different masses, a small relative momentum in the pair rest frame means that both particles have similar velocities in the laboratory frame and not similar momentum. This point is particularly important to realize when studying correlation involving pions. Due to the low pion mass, the pion velocity is the same as heavier particles (e.g., kaons or protons) when its momentum is much lower than the particle momentum it is associated with. For example, a proton with a momentum of 1 GeV/c has the same velocity as a pion with a momentum of $\approx$0.15 GeV/c.

As described in Ref. [78], the spatial separation between particles in the pair rest frame can be projected along three axes, $\langle r^*_{\rm out}\rangle$, along the pair transverse momentum, $\langle r^*_{\rm side}\rangle$, perpendicular to the pair transverse momentum and $\langle r^*_{\rm long}\rangle$, along the beam axis. To study the blast-wave prediction, we focus on the limiting case where the relative momentum between both particles in the pair rest frame is zero, which means that both particles have the same velocity. Thus we calculate the separation between particles 1 and 2 in the pair rest frame $\langle \Delta r^*_{\rm out}\rangle$, $\langle \Delta r^*_{\rm side}\rangle$, and $\langle \Delta r^*_{\rm long}\rangle$, at a given pair transverse velocity β_T, azimuthal angle ϕ_p, and longitudinal velocity β_L:

$$\langle \Delta r^*_{\rm out} \rangle = \langle r^*_{\rm out}(1) \rangle - \langle r^*_{\rm out}(2) \rangle, \tag{33}$$

$$\langle \Delta r^*_{\rm side} \rangle = \langle r^*_{\rm side}(1) \rangle - \langle r^*_{\rm side}(2) \rangle, \tag{34}$$

$$\langle \Delta r^*_{\rm long} \rangle = \langle r^*_{\rm long}(1) \rangle - \langle r^*_{\rm long}(2) \rangle, \tag{35}$$

with the particle emission points defined as (x,y,z,t)

$$\langle r^*_{\rm out} \rangle = \gamma_T [\langle x \rangle \cos(\phi_p) + \langle y \rangle \sin(\phi_p) - \beta_T \langle t \rangle], \tag{36}$$

$$\langle r^*_{\rm side} \rangle = \langle y \rangle \cos(\phi_p) - \langle x \rangle \sin(\phi_p), \tag{37}$$

$$\langle r^*_{\rm long} \rangle = \gamma_L \langle (z - \beta_L (t) \rangle. \tag{38}$$

Recalling that $\langle \beta_L \rangle = \langle z/t \rangle, \langle r^*_{\rm long}(i) \rangle = 0$. Following the notation of Eq. (25), the variables $\langle x \rangle, \langle y \rangle$, and $\langle t \rangle$ depend on β_T and on the particle mass (m) as

$$\langle x \rangle = \overline{\{x\}_{0,0}}(m, \beta_T), \tag{39}$$

$$\langle y \rangle = \overline{\{y\}_{0,0}}(m, \beta_T), \tag{40}$$

$$\langle t \rangle = \frac{\Delta \tau^2 + \tau_0^2}{\tau_0} \overline{\{1\}_{0,1}}(m, \beta_T). \tag{41}$$

The average values of x and y will vary with particle mass and particle transverse velocity, which yields separations between pions and kaons, pions and protons, and protons and kaons in the pair rest frame shown as in Fig. 35. The dashed and dotted lines show the contribution of the spatial $(\Delta r_{\rm out})$ and time (Δt) separation boosted to the pair rest frame along the pair transverse momentum, respectively; i.e., the dashed line shows $\langle \gamma_T \Delta r_{\rm out} \rangle$ and the dotted line represents $-\langle \gamma_T \beta_T \Delta t \rangle$. The solid line shows $\langle \Delta r^*_{\rm out} \rangle = \langle \gamma_T (\Delta r_{\rm out} - \beta_T \Delta t) \rangle$, the spatial separation in the pair rest frame. When boosting to the pair rest frame, time and spatial shifts in the laboratory frame add up due to their opposite signs. The largest (smallest) shift is obtained when the mass ratio between both species is the largest (smallest)—i.e., for pion-proton (kaon-proton) pairs.

In order to understand the behavior of $\Delta r^*_{\rm out}$, it is instructive to investigate how the average emission points in the laboratory frame $(\langle r_{\rm out} \rangle)$ of pions and kaons behave in various conditions as shown in Fig. 36. This figure shows the average emission points of pions and kaons in four different configurations: (1) The thin solid line shows the flow profile [Eq. (4)], which sets the emission point of particles when $T = 0$ GeV. (2) The dotted line is calculated assuming an infinite system—i.e., $\Omega(r, \phi_s) = 1$ and with $T = 0.1$ GeV. (3) The dashed line corresponds to a finite system as in Eq. (1), with $a_s = 0$ and (for illustration) an extremely low temperature $T = 0.01$ GeV. (4) The thick solid line is calculated using the standard parameters used in Fig. 36. Only in case (1) are pions and kaons emitted exactly at the same point. Since $T = 0$ GeV, all particles are always emitted at the same point as set by the flow profile. In case (2), particle emission points spread around the average emission defined by the flow profile. At small η there are as many particles emitted at large r—i.e., large ρ as at small r. But when $|\eta|$ is large, the term

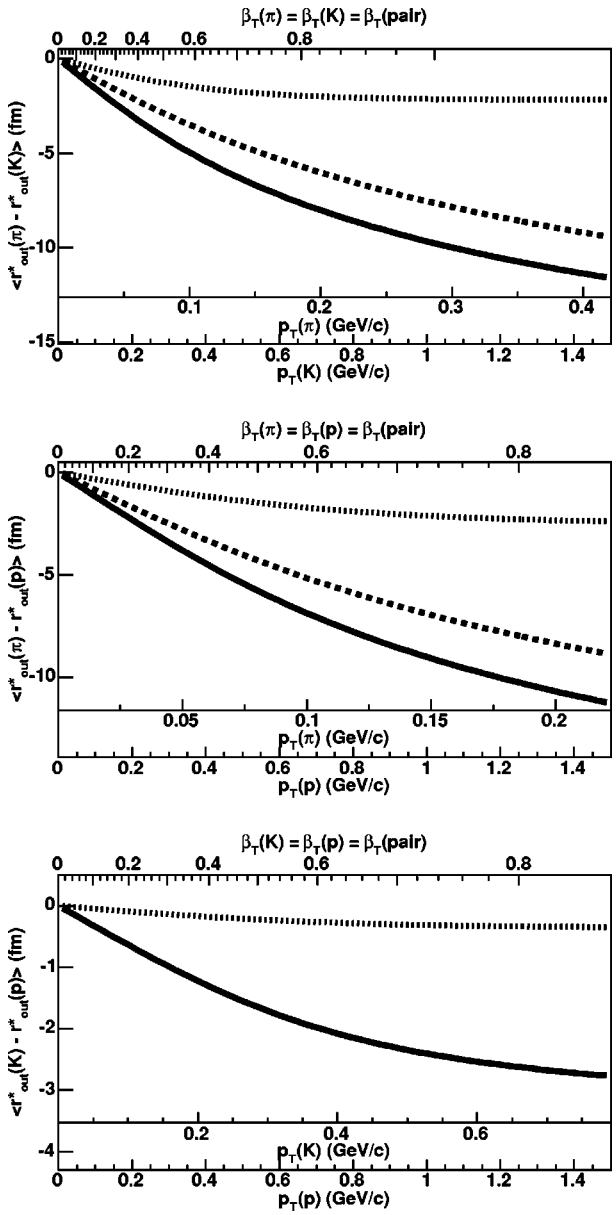

FIG. 35. Separation between the average emission points of pions, kaons, and protons in the pair rest frame along the pair transverse velocity. The values of the blast-wave parameters are for a round source, as listed in Table I. Dotted line: time shift in the laboratory boosted to the pair rest frame. Dashed line: spatial shift in the laboratory boosted to the pair rest frame. Solid line: total spatial shift in the pair rest frame.

$e^{-m_T/T \cosh \rho(r,\phi_s) \cosh(\eta)}$ in Eq. (12) favors small ρ—i.e., small r. Thus, the average emission point $\langle r_{\rm out} \rangle$ is smaller than the one defined by the flow profile. In case (3), the average emission points of pions and kaons follow closely the flow profile when the particle rapidity is significantly smaller than ρ_0. Close or beyond ρ_0, a certain fraction of the particle emission function is truncated due to the system finite size. The particle emission points are not allowed to spread beyond the system boundary, hence breaking the balance between particles emitted at small radii and particles emitted at large radii. Thus, the particle average emission radius is smaller

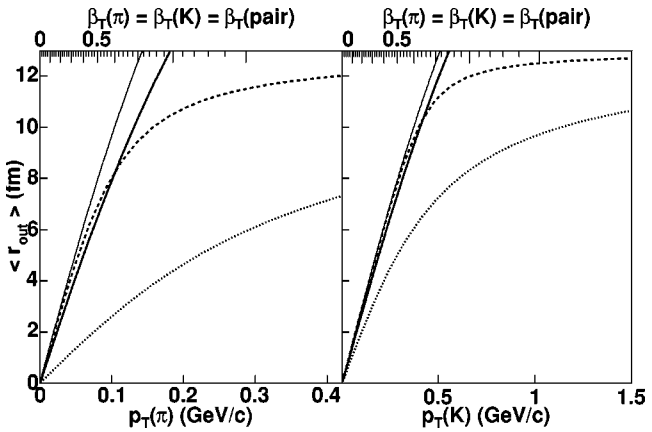

FIG. 36. Average emission points of pions (left) and kaons (right) as a function of the pion and kaon velocity and momentum. All curves are calculated with $\rho_0=0.9$ and $\rho_a=0$. The parameters τ and Δt are irrelevant. Thin solid line: $R_x=R_y=13$ fm, $T=0$ GeV. Thick solid line: infinite system [i.e., $\Omega(r,\phi_s)=1$], $T=0.1$ GeV. Dashed line: $R_x=R_y=13$ fm, $T=0.01$ GeV. Dotted line: $R_x=R_y=13$ fm, $T=0.1$ GeV.

than the emission radius given by the flow profile. Because the temperature is rather small, the average emission points of both species converge rapidly toward the radius of the system. The larger temperature in case (4) makes the average emission radii converge slowly toward the system limit. This phenomenon, with the addition of the phenomenon described in case (2), reduces very significantly the average particle emission radius compared to the flow profile limit.

The effect of temperature depends on particle mass and momentum. Random smearing is maximal for particles with low mass and momentum such as the low-p_T pions that are usually associated with kaons or protons in nonidentical particle correlation analyses. This effect is illustrated in Fig. 37. It shows the probability of emitting pions at a given point in the transverse plane for two different pion momenta $\vec{p}=(0.15,0,0)$ and $\vec{p}=(0.3,0,0)$. Kaon and proton momenta are calculated so that they have the same velocities as pions. The region of the system that emits particles of a given momentum shrinks and moves towards the edge of the system as the particle mass and/or momentum increases. The magnitude of the inward radius shift depends on the fraction of the source distribution that is truncated due to the system finite size. Thus, the inward shift of the average emission radius scales with the source size. This effect yields the systematic shift between the average emission points of pions, kaons, and protons as shown in Fig. 35 since the pion source size is the largest and the proton the smallest. Light particles are emitted the closer to the center of the source than heavier ones.

In addition to a spatial separation, the blast-wave parametrization induces a time shift between different particle species emitted at the same velocity as shown by the dotted line in Fig. 35. As a result of random motion, the space-time rapidity (η) spreads around the momentum rapidity (Y). Because the relationship $t=\tau\cosh(\eta)$ is positive definite, the larger dispersion of η for pions than for kaons or protons leads to a delay of the emission of pions with respect to

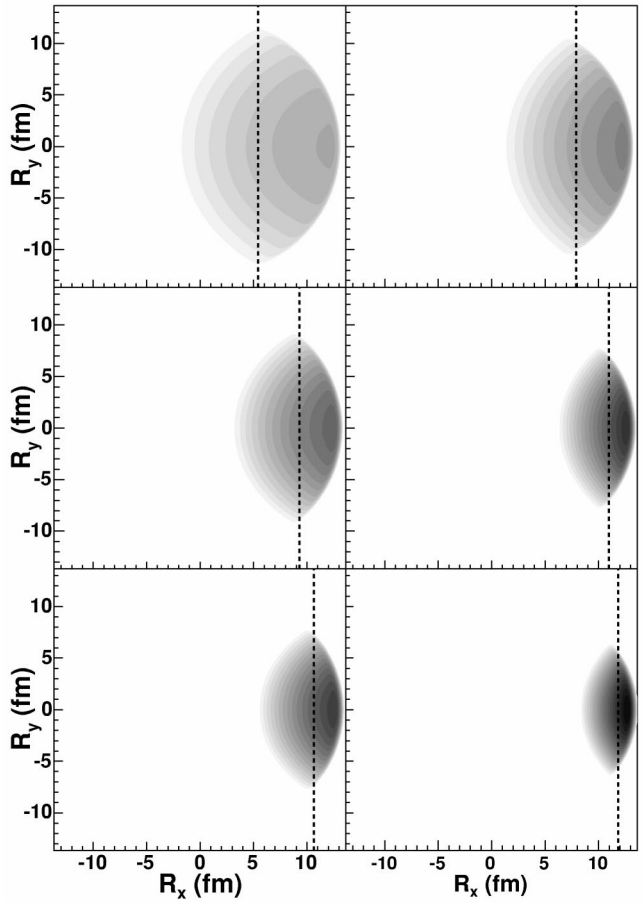

FIG. 37. Distribution of the emission points in the transverse plane, for different particle species emitted at the same velocity, $\beta_y=0$ and $\beta_x=0.907$ on the left-hand side and $\beta_x=0.974$ on the right-hand side. Top panels are for pions, middle for kaons and bottom for protons. The same logarithmic color scale is used for all six panels. The blast-wave parameters are the same as in Fig. 36 except that $a_s=0.01$. The dashed lines show $\langle x\rangle$.

kaons or protons. Protons are emitted first, then kaons, and then pions. The spatial and time shifts have opposite signs in the laboratory frame but they sum up when boosting to the pair rest frame. The solid line in Fig. 35 shows the added contributions of both shifts. The pion-kaon and pion-proton separation in the pair rest frame ranges from 5 to 15 fm, while the separation between kaons and protons is on the order of 2–4 fm. These shifts are large enough to be measured.

The curves in Fig. 35 have been obtained by setting the blast-wave parameters to arbitrary values. We will now investigate how changing these parameters affects the shift between pions and kaons. The results obtained studying pion-kaon separation can be easily extrapolated to pion-proton and kaon-proton separations. Since experimental analyses of nonidentical two-particle correlations performed to date do not investigate the azimuthal dependences with respect to the reaction plane, we will focus our study on central collisions. We will then show that the shift between the average emission points of different particle species oscillates with respect to the reaction plane without investigating the effect of varying the parameters in detail.

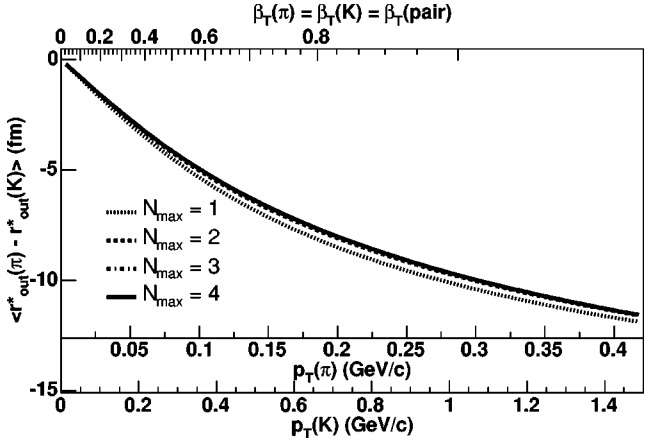

FIG. 38. Average separation between π and K in the pair rest frame as a function of the pion and kaon momenta using several values of N, the maximum value of n taken in the summation of Eq. (8). Values of the blast-wave parameters are for a round source, as listed in Table I.

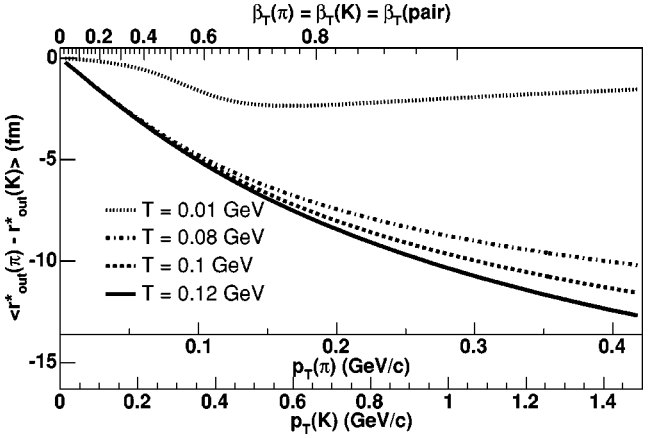

FIG. 39. Average separation between π and K in the pair rest frame as a function of the pion and kaon momenta for different temperature. The values of the other blast-wave parameters are for a round source, as listed in Table I.

2. Nonidentical particle correlations in central collisions

In central collisions, azimuthal symmetry implies that the particle emission pattern depends only on the relative angle between the position and momentum $\phi_p - \phi_s$. Thus, setting for convenience $\phi_p = 0$ yields

$$\langle r^*_{\rm out}(i)\rangle = \langle \gamma_T (x_i - \beta_T \Delta t_i)\rangle, \tag{42}$$

$$\langle r^*_{\rm side}(i)\rangle = 0. \tag{43}$$

Furthermore, we consider emission from an azimuthally isotropic source ($R_x = R_y$ and $\rho_2 = 0$) only. Hence, the only quantity of interest is $\langle \Delta r^*_{\rm out}\rangle$.

Figure 38 shows the dependence of the average separation between π and K in the pair rest frame as a function of the pion and kaon momentum using several values of N, the maximum value of n taken in the summation of Eq. (8). Pions and kaons are of course treated as bosons. The difference between the average separation calculated either by using a Boltzmann function ($N=1$) or by approximating the Bose-Einstein distribution at the fourth order is smaller than 0.5 fm. The maximum relative difference is on the order of 8% at small transverse momentum. The Bose-Einstein distribution already converges when $N=2$.

Figure 39 shows the dependence of the spatial shift between pions and kaons in the pair rest frame as a function of the pair velocity for different temperature. The shift increases as the temperature increases all the way from 0.01 GeV to 0.12 GeV. When the temperature is very low (e.g., 0.01 GeV), pion and kaon emission patterns are dominated by space-momentum correlation independent of particle masses. In the limit of zero temperature, there is a unique correspondence between the particle velocity and emission point. In that case, since we consider particles with the same velocity, pions and kaons are emitted from the same point. On the other hand, when the temperature is nonzero, a fraction of the pions and kaons that would be emitted in an infinite system are truncated, which shifts their average emission points inward. Because the pion source size is significantly larger than the kaon source size due to the pion lower mass and momentum, the pion average emission point is more shifted inward than the kaon's, which is illustrated in Fig. 40. This figure shows the contribution of the spatial shift in the average separation between the pion and kaon average emission points in the pair rest frame. When the temperature is low (0.01 GeV), both spatial and time separations are small as shown by the dashed lines in Figs. 40 and 41. As the temperature increases, the pion emission time increases faster than the kaon emission time; the higher the temperature, the larger the shift between pion and kaon average emission time (after boosting into the pair rest frame). On the other hand, the spatial shift varies little within the temperature range expected in relativistic heavy-ion collisions (0.08–0.12 GeV). At a temperature above 10 MeV/c, a fraction of the pion and kaon sources is truncated even at low particle velocity. The fraction of the source that is truncated, which

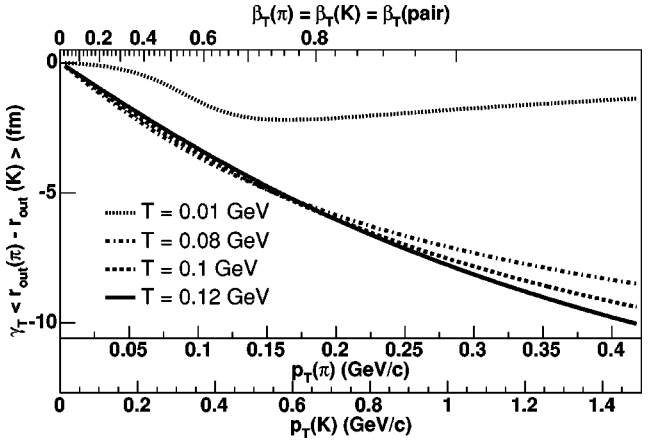

FIG. 40. Contribution of the spatial shift to the average separation between pions and kaons in the pair rest frame as a function of the pion and kaon momenta for different temperature. The values of the other blast-wave parameters are for a round source, as listed in Table I.

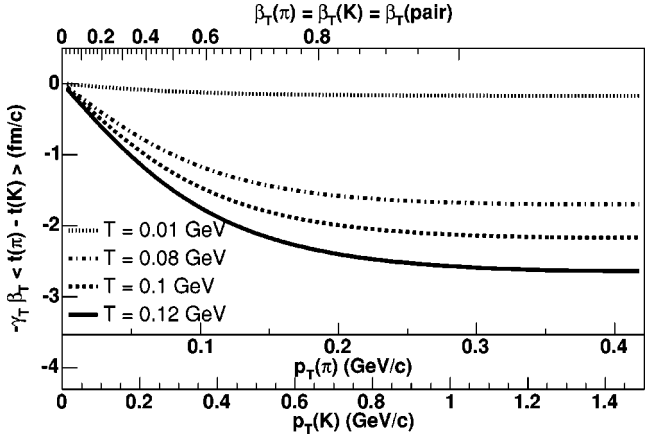

FIG. 41. Contribution of the time shift to the average separation between pions and kaons in the pair rest frame as a function of the pion and kaon momenta for different temperature. The values of the other blast-wave parameters are for a round source, as listed in Table I.

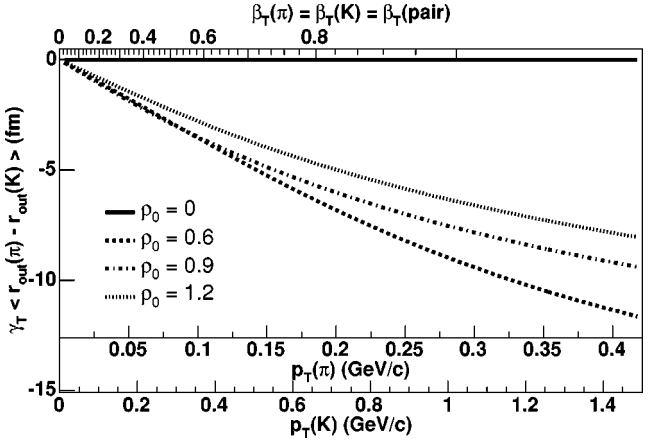

FIG. 43. Contribution of the spatial shift to the average separation between pions and kaons in the pair rest frame as a function of the pion and kaon momenta for different flow rapidity (ρ_0). The values of the other blast-wave parameters are for a round source, as listed in Table I.

leads to an inward shift of the average emission radius, varies with transverse momentum and particle mass but it is relatively insensitive to temperature variation between 0.08 and 0.12 GeV. It is interesting to note that the average spatial separation between pions and kaons in the laboratory frame actually decreases as the particle velocity rises above $0.8c$. However, this decrease is not visible in Figs. 39 and 40 because the γ_T factor applied when boosting to the pair rest frame rises faster with velocity than the separation between pions and kaons in the laboratory frame decreases.

Changing the maximum flow rapidity (ρ_0) also affects the separation between pions and kaons in the pair rest frame as shown in Fig. 42. When $\rho_0=0$, pions and kaons are emitted from the same space point as shown in Fig. 43 and only the time shift remains (Fig. 44). Indeed, the time shift depends weakly on ρ_0. Figure 44 shows that the contribution of the time shift to the separaration between pions and kaons in the pair rest frame reaches a plateau when the pion momentum reaches 0.25 GeV/c. The magnitude of the time shift starts decreasing in the laboratory frame upon reaching this pion momentum but it is compensated by an increase of the boost factor $\gamma_T\beta_T$. On the other hand, when ρ_0 is large enough, a significant spatial separation appears in the pair rest frame, which is sensitive to the value of ρ_0. The main effect of increasing the flow strength is to decrease the pion (and kaon) transverse source size, as shown in Fig. 31. In the laboratory frame, the spatial shift between pion and kaon average emission point switches from decreasing to increasing as the particle velocity increases. The value of the velocity where this switch occurs depends on the value of ρ_0. The increase of the spatial shift between pions and kaons arises from two effects: the first is the expected shift of the average emission point of both particles due to the flow profile; the second is that the kaon source size drops more rapidly than the pion source size. Then, above a velocity that depends on

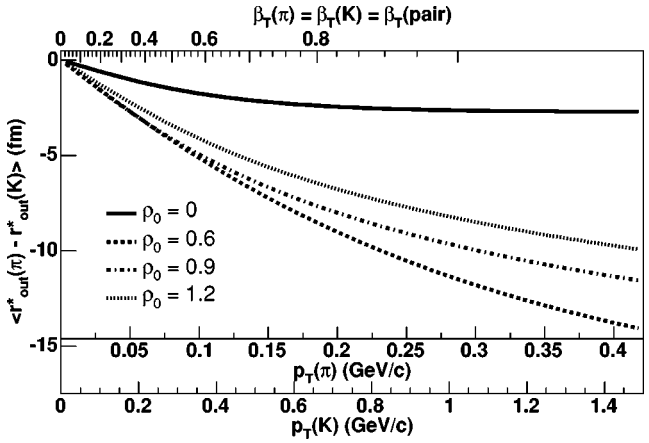

FIG. 42. Average shift between the pion and kaon emission points in the pair rest frame as a function of the pion and kaon momenta for different flow rapidity (ρ_0). The values of the other blast-wave parameters are for a round source, as listed in Table I.

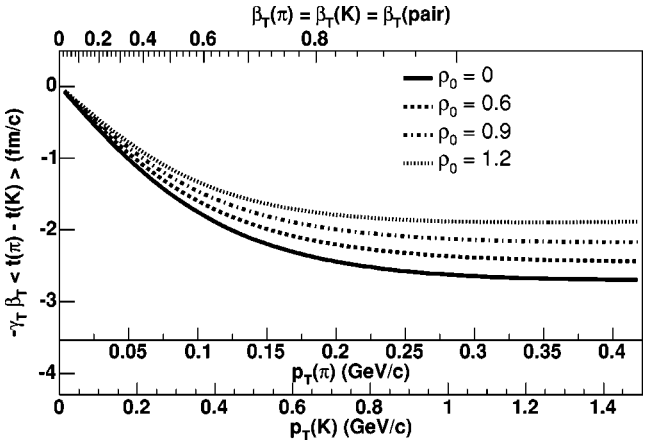

FIG. 44. Contribution of the time shift to the average separation between pions and kaons in the pair rest frame as a function of the pion and kaon momenta for different flow rapidity (ρ_0). The values of the other blast-wave parameters are for a round source, as listed in Table I.

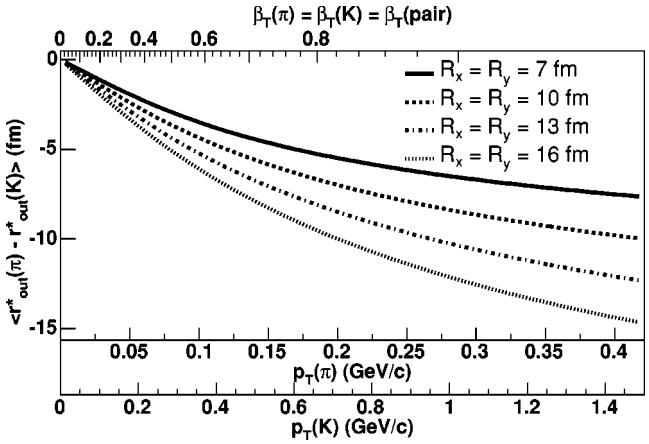

FIG. 45. Average shift between the pion and kaon emission points in the pair rest frame as a function of the pion and kaon momenta for different system radius ($R_x = R_y$). The values of the other blast-wave parameters are for a round source, as listed in Table I.

ρ_0, the fraction of pion that would be emitted beyond the system limit starts dropping faster than the corresponding fraction of kaons, and thus the separation between the average emission points of pions and kaons decreases. However, this turnover, which takes place in the laboratory frame, is not directly visible in Fig. 43 because the boost factor γ_T compensates it.

Figure 45 shows the sensitivity of the average separation between pion and kaon emission point in the pair rest frame to varying the system radius. This spatial separation scales directly with the system radius because it does not modify the fraction of pions or kaons that are truncated due to the system finite size.

Like the system radius, the proper lifetime τ_0 acts as a scale driving the shift between the pion and kaon emission times. Figure 46 shows the effect of varying τ_0 on the separation between pions and kaons in the pair rest frame. The

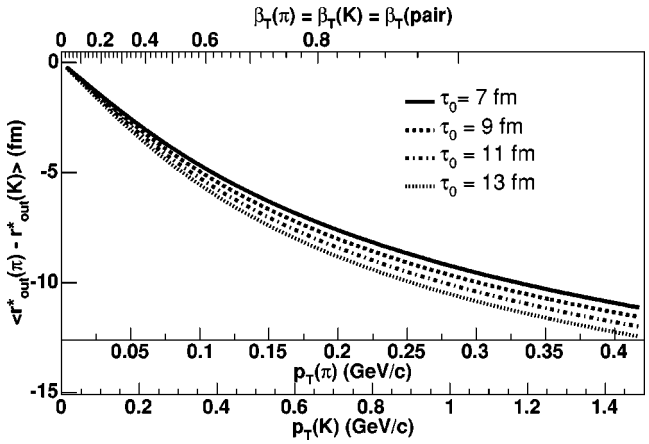

FIG. 46. Average shift between the pion and kaon emission points in the pair rest frame as a function of the pion and kaon momenta for different system proper lifetime (τ_0). The values of the other blast-wave parameters are for a round source, as listed in Table I.

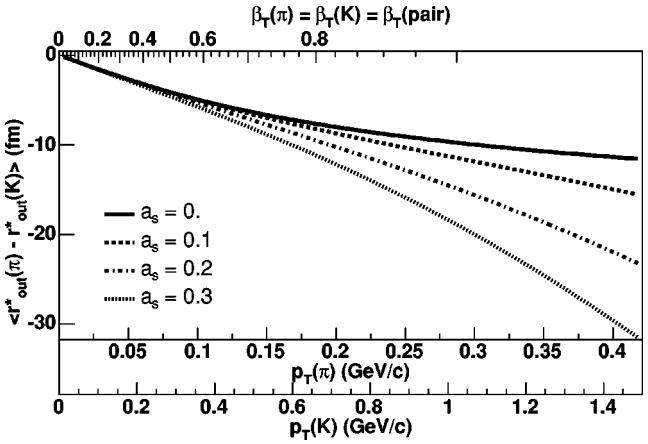

FIG. 47. Average shift between the pion and kaon emission points in the pair rest frame as a function of the pion and kaon momenta for surface smoothness (a_s). The values of the other blast-wave parameters are for a round source, as listed in Table I.

effect of varying τ_0 is small because the contribution of the time shift to the separation in the pair rest frame is significantly smaller than the contribution of the spatial separation.

Figure 47 shows the effect of varying a_s on the separation between pions and kaons in the pair rest frame. Unlike in Fig. 34, ρ_0 was kept constant. Indeed varying ρ_0 significantly affects the average emission radii, which hides the effect of changing a_s at low velocity. However, when the velocity is larger than $\tanh(\rho_0) = 0.716c$, the amount of boost and space-momentum correlation that a particle acquires depends on a_s; the larger a_s, the larger the boost. Thus, when the pair velocity is lower than $0.716c$, the separation decreases with increasing a_s because the fraction of truncated particles decreases. When the pair velocity is larger than $0.716c$, increasing a_s has the same consequence as increasing ρ_0.

3. Nonidentical particle correlations in noncentral collisions

As reported in Ref. [73], the average space-time separation between different particle species may depend on the particle emission angle with respect to the reaction plane. The effect in the blast-wave parametrization is shown in Fig. 48. The blast-wave parameters are the same as in Fig. 35 with the exception of R_x and ρ_2 which are varied. Clear oscillations of $\langle r^*_{\rm out}(\pi) - r^*_{\rm out}(K)\rangle$ are found when R_x is set to 11 fm—i.e., when the source is out-of-plane extended ($R_y = 13$ fm). Small oscillations of $\langle r^*_{\rm side}(\pi) - r^*_{\rm side}(K)\rangle$ appear as well. The oscillations in both directions are on the order of 1–2 fm, which may be measurable. On the other hand, keeping the source cylindrical but setting the flow modulation parameter ρ_2 to 0.05 yields very small oscillations, which will be very challenging to probe experimentally. Thus, nonidentical two particle correlation analyses with respect to the reaction plane, as the pion HBT measurement may provide a good handle on the source shape but not on the flow modulation.

E. Summary of the effects of parameters

Above, we have explored the sensitivity of several experimental observables on various freeze-out parameters. Here,

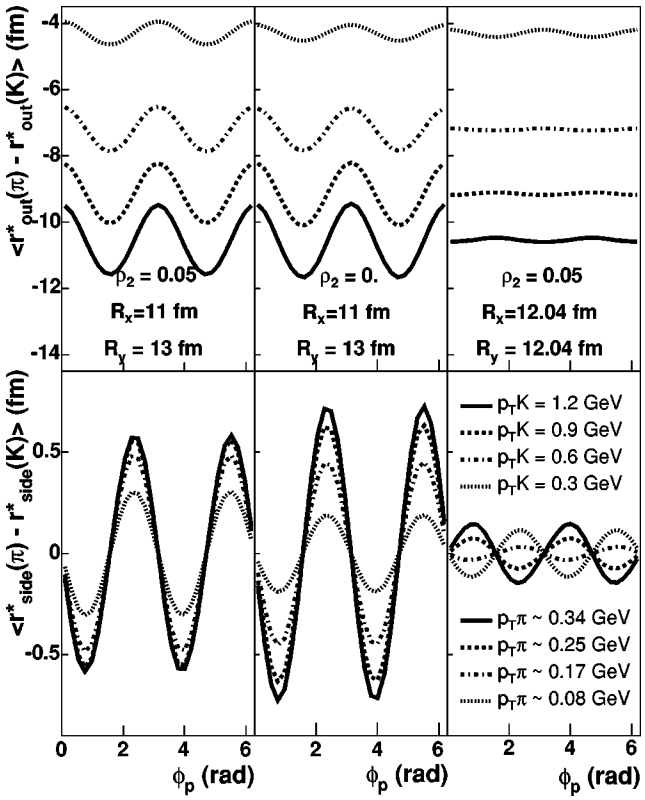

FIG. 48. Average separation between pions and kaons in the pair rest frame as a function of their momentum azimuthal angle with respect to the reaction plane. The four different lines are calculated for four different kaon momenta and the corresponding four different pion momenta required so that pions and kaons have the same velocity. The values of the blast-wave parameters used in the left panel are for a "nonround" source, as listed in Table I. The same parameters were used in the middle panel except that $\rho_2=0$. The round source parameters are used in the right panel except that $\rho_2=0.05$. The separation along the *out* and *side* axes is shown in the upper and lower panels, respectively.

we summarize in an orthogonal manner, describing briefly the main observable effects due to an increase in each parameter, if the other parameters are left fixed.

The temperature parameter T quantifies the randomly oriented kinetic energy component of the freeze-out scenario. Increasing this energy component leads to decreased slopes of p_T spectra, especially for light-mass particles. Since random motion destroys space-momentum correlations, increasing T reduces measured elliptic flow (v_2) and increases homogeneity scales—i.e., $R^2_{\mu,0}$. On the other hand, for the range of values considered, increasing temperature increases the average separation in the pair rest frame between pions and heavier particles—e.g., $\langle r^*_{\rm out}(K) - r^*_{\rm out}(\pi)\rangle$.

The ϕ-averaged transverse flow strength is quantified in this model by ρ_0. Increasing this directed energy component decreases slopes of p_T spectra, especially for heavier particles. Increasing ρ_0 leads to increasing space-momentum correlations, which reduce $R^2_{\mu,0}$ and $\langle r^*_{\rm out}(K) - r^*_{\rm out}(\pi)\rangle$, and at constant ρ_2 reduces v_2 at high m_T.

The parameter a_s quantifies the "surface diffuseness" of the spatial density profile. Taking care to keep the average transverse flow fixed, variation in a_s has little effect on purely momentum-space observables: p_T spectra and $v_2(m,p_T)$. On the other hand, going from a "box profile" ($a_s=0$) to a pseudo-Gaussian profile ($a_s=0.3$) increases the "out-to-side" ratio $R^2_{o,0}/R^2_{s,0}$ at higher p_T, as the homogeneity region is not constrained by hard geometric "emission boundaries." Furthermore, for a fixed average transverse flow (and flow gradient), increasing a_s leads to stronger oscillations in the HBT radius parameters. Increasing a_s also increases the $\langle r^*_{\rm out}(K) - r^*_{\rm out}(\pi)\rangle$ when the temperature and particle velocity are such that the pion source size is significantly larger than the kaon's.

Considering variations in the geometric transverse scale of the source $\sqrt{R_x^2+R_y^2}$, while keeping all else (including R_y/R_x) constant, we conclude that the sensitivity is in the HBT radii and the average separation between different particle species. In HBT measurements, the sensitivity to this parameter is through $R^2_{o,0}$ and $R^2_{s,0}$. The spatial shifts that contribute to the separation $\langle r^*_{\rm out}(K) - r^*_{\rm out}(\pi)\rangle$ in the pair rest frame scale directly with this parameter. Momentum-space observables such as spectral shapes or v_2 are unaffected.

We turn now to variations in the time scale parameters—the evolution duration (τ_0) and emission duration ($\Delta\tau$). The only significant variations are in $R^2_{l,0}$ and $R^2_{o,0}$, and these depend differently on τ_0 and $\Delta\tau$, allowing independent probes of the two parameters. The time shifts that contribute to the separation $\langle r^*_{\rm out}(K) - r^*_{\rm out}(\pi)\rangle$ in the pair rest frame scale directly with these parameters (τ_0 and/or $\Delta\tau$).

Noncentral collisions may exhibit azimuthally anisotropic geometry and/or dynamics in the freeze-out configuration. These two effects were studied by varying R_y/R_x and ρ_2, respectively. Azimuthally integrated p_T spectra were negligibly affected, as were the ϕ_p-averaged values of HBT radii ($R^2_{\mu,0}$). Observables designed to probe anisotropy, v_2, and $R^2_{\mu,2}$ of course showed strong sensitivity to geometric or dynamical anisotropy, increasing strongly in magnitude as R_y/R_x deviates from unity and/or ρ_2 from zero.

IV. COMPARISON WITH EXISTING DATA

In the previous section, we reviewed the various experimental observables that the blast-wave parametrization may be able to reproduce. The effect of changing blast-wave parameters has been examined. In this section, we investigate how well those parameters can be constrained by the experimental data.

Before comparing the blast-wave parametrization with data, we highlight its limitations and possibly not valid assumption.

(i) *Freeze-out from a thermalized system at a constant temperature*. In the blast-wave framework, freeze-out is assumed to take place at the same temperature for every particle. In principle, this condition may be relaxed by fitting separately the data for each type of particle. (We do not attempt this here.) Perhaps a more important assumption, however, is made in discussing "temperature" at all; it requires system thermalization. If particles are emitted in a nonthermal way, our framework may fail to describe the data.

TABLE II. Upper section: data used in the fit. Middle section: number of χ^2/data points for each measure. Lower section: best fit parameters. Note that $\langle\beta_T\rangle$ is not a fit parameter, but it is calculated from ρ_0.

	Central	Midcentral	Peripheral
Data			
π, K, p spectra [81]	0%–5%	15%–30%	60%–92%
Λ spectra [82]	0%–5%	20%–35%	35%–75%
Pion radii [70]	0%–12%	12%–32%	32%–72%
Elliptic flow [37]	0%–11%	11%–45%	45%–85%
χ^2/(number of data points)			
π^+, π^- spectra	7.2/10	26.5/10	13.0/9
K^+, K^- spectra	24.2/22	21.4/22	10.1/10
$p, \bar{p}$ spectra	10.6/18	23.2/18	28.0/12
$\Lambda, \bar{\Lambda}$ spectra	9.5/16	12.8/16	11.0/16
$\pi\ v_2$	14.6/12	29.8/12	5.2/12
$p\ v_2$	1.6/3	9.2/6	0.8/3
$\pi\ r_{\mathrm{out}}$	1.9/6	0.4/2	0.4/2
$\pi\ r_{\mathrm{side}}$	2.7/6	0.07/2	0.06/2
$\pi\ r_{\mathrm{long}}$	5.3/6	0.003/2	0.1/2
Total	77.6/99	107.7/90	68.7/68
Parameters			
T (MeV)	106±3	107±2	100±5
ρ_0	0.89±0.02	0.85±0.01	0.79±0.02
$\langle\beta_T\rangle$	0.52±0.01	0.50±0.01	0.47±0.01
ρ_2	0.060±0.008	0.058±0.005	0.05±0.01
R_x (fm)	13.2±0.3	10.4±0.4	8.00±0.4
R_y (fm)	13.0±0.3	11.8±0.4	10.1±0.4
τ (fm/c)	9.2±0.4	7.7±0.9	6.5±0.6
Δt (fm/c)	0.003±1.3	0.06±1.3	0.6±1.8

(ii) *Longitudinal boost invariance*. The blast-wave parametrization relies on longitudinal boost invariance. Elliptic flow data (v_2) published by the PHOBOS Collaboration clearly show that longitudinal boost invariance is broken for rapidity larger than 1 [79]. Thus the blast-wave parametrization can only be applied within $|Y|<1$. This assumption will be validated or ruled out by high-precision data.

(iii) *No resonances*. The observables that constrain the blast wave are calculated for each particle species using their own masses, ignoring the fact that some particles may be decay products of other particles. In fact a large fraction of pions and protons produced at RHIC energy originates from resonance decays. As mentioned in Sec. III, pions from ω meson decay distort the pion source space-time distribution but this effect is limited because the fraction of pions coming from ω is on the order of 10%. On the other hand, pion spectra and to a lesser extent proton spectra may be significantly distorted by resonance feeddown. Within the blast-wave framework, however, it was found in [30,80] that accounting for resonances affects the blast-wave-parameter-extracted fit to spectra by no more than 20%. While 20% is not negligible, we feel that the gross features of the parametrization are preserved. On the other hand, an investigation of the effect of resonance feeddown on v_2 remains to be performed.

We focus on data from Au-Au collisions at $\sqrt{s_{NN}}=130$ GeV published by the PHENIX and STAR Collaborations at RHIC. The measurements used are listed at the top of Table II. To avoid uncertainties between different experiments and to optimize the overlap between centrality bins, we do not use the full set of data published at RHIC. Three centrality bins are available. The approximate overlap between the centrality bins for the different measures may affect the quality of the fits.

The blast-wave parameters are constrained by simultaneously fitting transverse momentum spectra, transverse momentum azimuthal anisotropy (v_2), and pion HBT radii. Bose-Einstein and Fermi-Dirac distributions are used when appropriate using the approximation to the fourth order as in Eq. (8)—i.e., the value of $n=4$ in the summation of Eq. (8). The quality of the fit to each measure is shown by the χ^2 per data points listed in Table II. The number of degrees of freedom is not shown because the number of parameters cannot be subtracted from the number of data points independently for each measure. In addition to the seven blast-wave parameters, there are eight scaling parameters used to normalize π^+, π^-, K^+, K^-, p, $\bar{p}$, Λ, and $\bar{\Lambda}$ spectra. These scaling parameters (A) are not minimized by the fitting function but calculated directly. The χ^2 for a given spectra is given by

$$\chi^2 = \sum_i \left(\frac{d_i - Ac_i}{e_i} \right)^2, \tag{44}$$

where d_i is the measured invariant yield in bin i. Here e_i is the experimental error on d_i, and c_i is the calculated invariant yield. The χ^2 minimum occurs when $d\chi^2/dA=0$, and hence

$$A = \frac{\sum_i d_i c_i / e_i^2}{\sum_i c_i / e_i^2}. \tag{45}$$

To avoid the region where resonance feeddown may be large and where the Boltzmann approximation may not be valid, fits to transverse momentum spectra are restricted to pions with $p_T > 0.4$ GeV/c. We further restrict the fit range to $p_T < 1$ GeV/c for pions, $p_T < 1.5$ GeV/c for kaons, and $p_T < 2$ GeV/c for protons and lambdas, because hard processes may significantly contribute to the particle yield above these momenta [28].

Given the large number of data points from the spectra, the temperature (T) and the maximum flow rapidity (ρ_0) parameters are constrained by transverse mass spectra. A comparison of the data and the blast-wave calculation with the best fit parameters is shown in Fig. 49. In semilogarithmic plots, the data and the model fits seem to agree very well. The χ^2/(number of data points) in Table II shows, however, that the fit quality varies between particle species and centrality bins. The correlation between the flow rapidity and temperature is shown in Fig. 50. The extracted temperatures and flow velocities are consistent with similar studies reported in Refs. [29–31,83]. The differences between these analyses are due to the use of different data sets, different fit ranges, and different flow and spatial profiles. The study reported in Ref. [30] shows that accounting for resonance feeddown leads to a temperature 30% higher and a transverse velocity 15% lower than in our study.

The fit of v_2 mainly constrains the flow rapidity modulation parameter ρ_2 and the ratio between the radius in plane and out of plane, R_x/R_y. A comparison between the data and the blast-wave calculation with the best fit parameters is shown in Fig. 51. The correlation between ρ_2 and R_x/R_y is shown in Fig. 52. The fit performed in this paper differs from the fit reported together with the data in Ref. [37]. There are three main differences: (i) in Ref. [37], the temperature and flow velocity are free parameters while in this paper they are mostly determined by spectra shapes, (ii) a filled volume and a flow profile are used instead of a shell, and (iii) the fits are performed on three centrality bins instead of the minimum-bias sample. Thus, a direct comparison between the fit parameters extracted in this paper and those reported in Ref. [37] is difficult. The freeze-out spatial anisotropy probed by the ratio R_x/R_y increases when increasing the initial state spatial anisotropy—i.e., when going from central to peripheral events. The flow modulation decreases from central to peripheral events, following the same trend as ρ_0.

The pion source radii allow us to estimate the parameters R_x (or R_y), τ, and Δt. As discussed earlier, the ratio R_x/R_y is constrained by the fit to v_2. In the midperipheral and peripheral bins, the pion source size has been measured at only one transverse momentum, which weakly constrains the parameters. The comparison between the data and the blast-wave calculation performed with the best fit parameters is shown in Fig. 53. This figure includes the pion source radii reported by the PHENIX Collaboration [59] although they were not used in the fit. These radii were measured over the 30% most central events, which does not overlap well with the STAR Collaboration centrality bins (0–12 %, 12–32 %, and 32–72 %). Qualitatively the PHENIX data points agree with the blast-wave fit as they oscillate between the central and midperipheral lines. The χ^2 obtained from the fit is small, because the systematic errors were added in quadrature to the statistical errors. The system radius increases from peripheral events to central events following the growth of the system initial state. The final system radius is roughly twice the initial system radius, which is clear evidence of the system expansion. The proper time (τ) is surprisingly small. Typically, hydrodynamical calculations reach kinetic freeze-out in 15 fm/c, not 9 fm/c [84]. The hydrodynamical calculations may be over-predicting the system lifetime or the assumption underlying the extraction of τ may not be valid. The assumption of a boost-invariant expansion along the beam axis from a narrow (less than 1 fm thick) pancake may

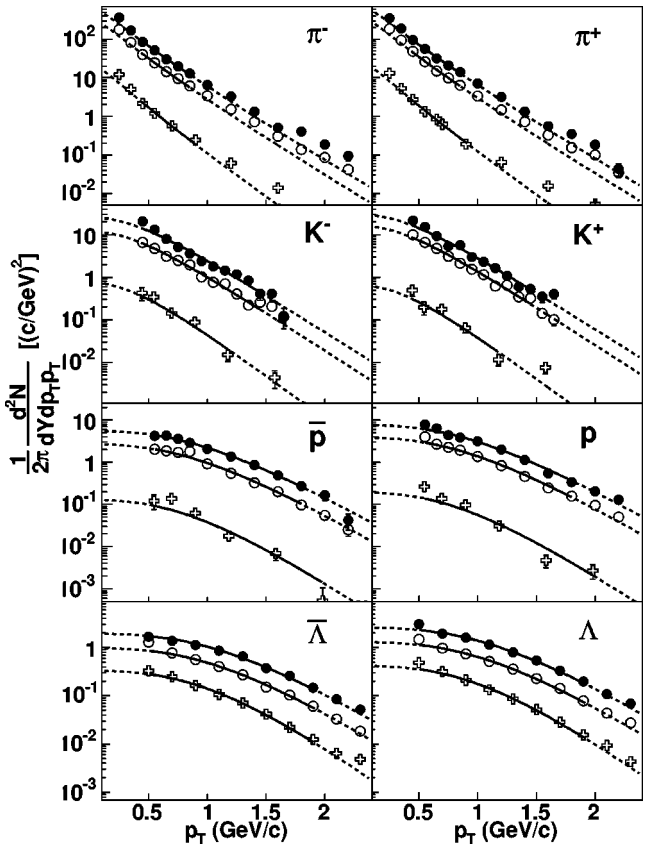

FIG. 49. Comparison of the data with the blast-wave calculations performed with the best fit parameters in three centrality bins. The solid circles are central data, the open circles are midcentral data, and the crosses are peripheral data. The solid lines show the blast-wave calculation within the fit range while the dashed lines show the extrapolation over the whole range.

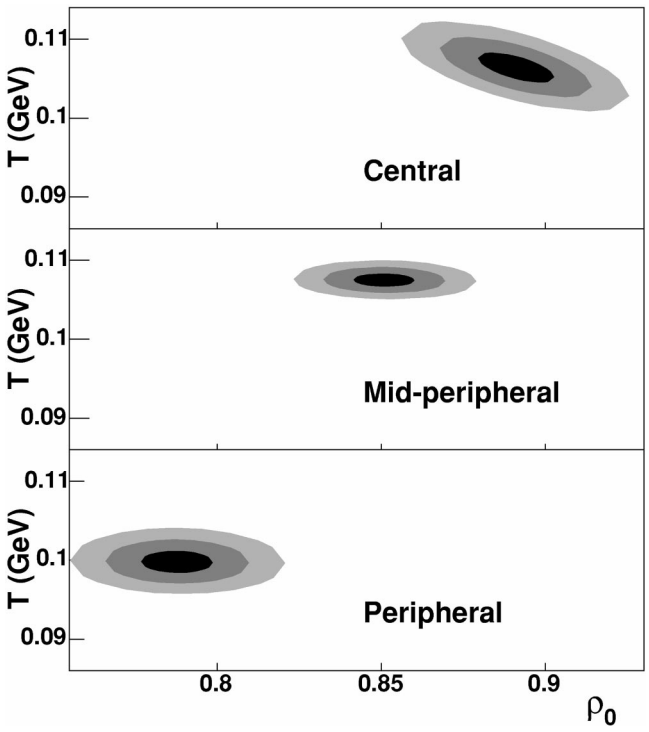

FIG. 50. Number of σ contour of the maximum flow rapidity (ρ_0) with respect to the temperature (T). The shadows show the 1σ, 2σ, and 3σ contours from darkest to lightest.

be too simplistic. Indeed, it has been shown that accounting for the fluid viscosity breaks the boost-invariant flow [25]. Furthermore, three-dimensional hydrodynamical calculations reproduce the measured pseudorapidity distribution only when the initial width of the system along the beam axis extends over several units of spatial pseudorapidity [85]. Such initial conditions lead to a longitudinal expansion that also breaks boost-invariant scaling. In these calculations, even though the system persists for 15 fm/c, the R_{long} radii are well reproduced. Thus, the absolute value of the proper lifetime τ extracted within the blast-wave parametrization may be questionable. Along the same lines, the very short emission duration is surprising. Indeed, a scenario where particles are emitted in a flash would appear rather unlikely. (On the other hand, processes such as supercooling [86] have been discussed and may lead to such a scenario.) Recent experimental data [87] show that the value of the R_{out} radius may have been underestimated by the experiments. Thus, since the emission duration parameters Δt strongly depend on R_{out}, it is not appropriate to draw definite conclusions until the experimental issues are settled.

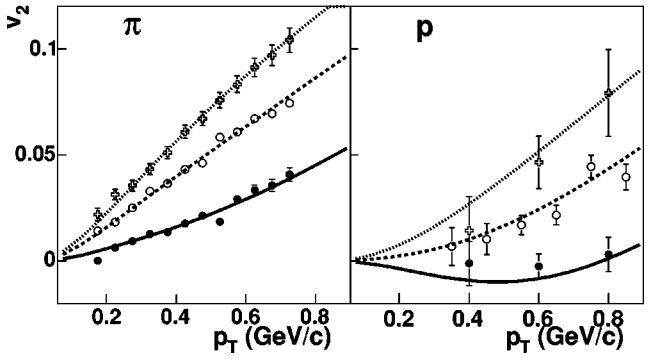

FIG. 51. Comparison of the v_2 data with the blast-wave calculations performed with the best fit parameters in three centrality bins. The solid circles are central data, the open circles are midcentral data, and the crosses are peripheral data.

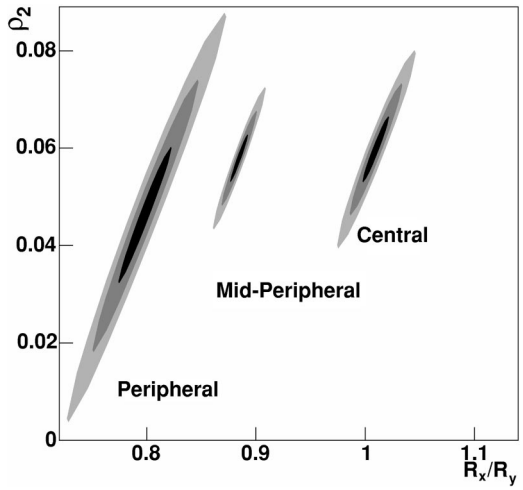

FIG. 52. Number of σ contours of the ratio of the in-plane radius over the out-of-plane radius (R_x/R_y) with respect to the flow rapidity oscillation parameter (ρ_2). The colors show the 1σ, 2σ, and 3σ contours from darkest to lightest.

We have shown that $\pi, \mathrm{K}, p, \Lambda$ transverse momentum spectra, π, p elliptic flow, and pion source radii measured in Au-Au collisions at $\sqrt{s_{NN}}=130$ GeV are well reproduced by

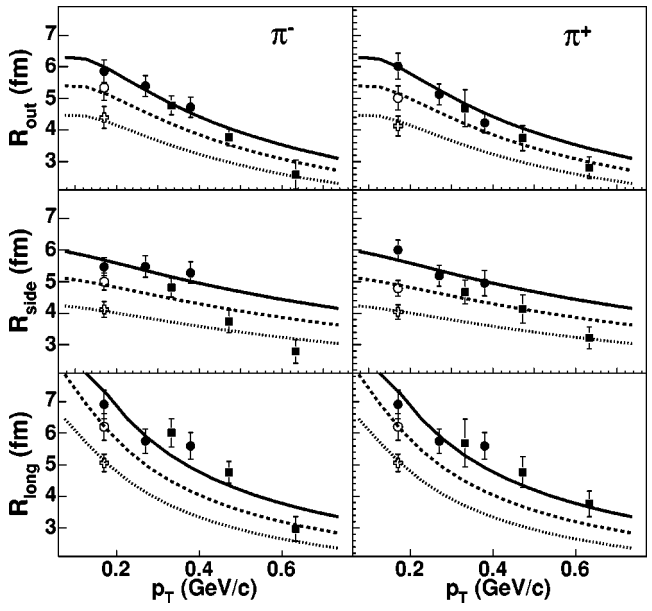

FIG. 53. Comparison of the pion source data measured by the STAR (circle) and the PHENIX (box) Collaborations with the blast-wave calculations. Only the STAR data were used to constrain the blast-wave parameters. The solid circles are the central data, the open circles are the midcentral data, and the crosses are peripheral data.

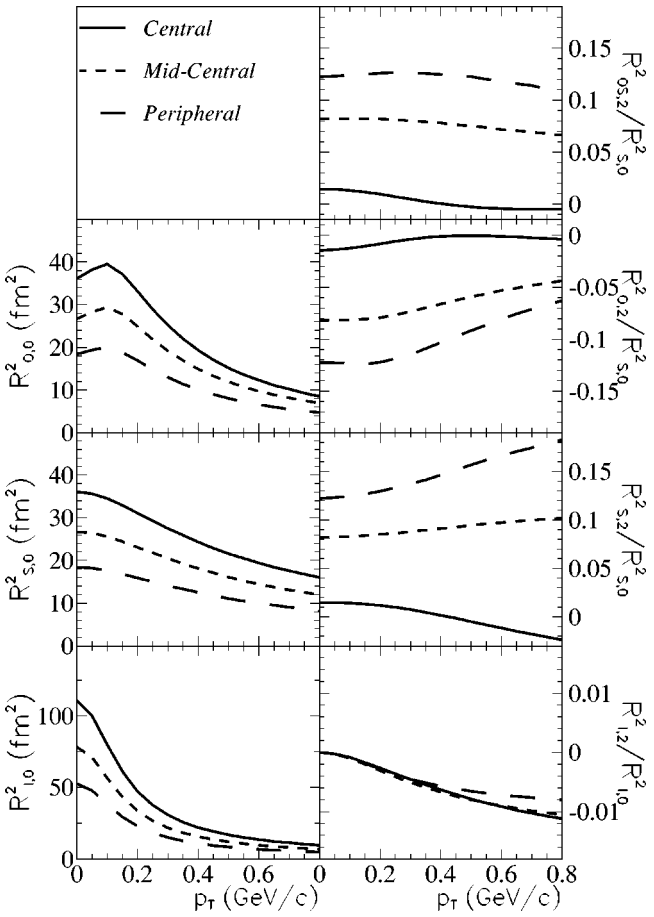

FIG. 54. Oscillations of the pion source radii obtained with the best fit parameters in the three centrality bins.

the blast-wave parametrization. With the exception of the time-scale parameters (system proper lifetime and emission duration), which fall short of any realistic model calculations, the fit parameters are within expectations. This issue may be resolved when new data on pion source radii become available. Based on the published data in Au-Au collisions at $\sqrt{s_{NN}}$=130 GeV, we conclude that the blast-wave parametrization provides a good description of the system freeze-out stage.

This conclusion will be tested in the future, using the sensitivity of the blast-wave parametrization to observables that have been presented in the previous section: the oscillation of the pion radii with respect to the reaction plane and the space-time separation between the emission points of different particle species. Using the parameters extracted from the fits we have calculated the corresponding oscillation of the pion radii with respect to the reaction plane (Fig. 54) and the separations between the average space-time emission point of pions, kaons, and protons (Fig. 55). We have also calculated the kaon source radii as shown in Fig. 56 since they may become available from the RHIC experiments [87,88]. The blast-wave parametrization faces the challenge of simultaneously reproducing a large variety of observables that will be measured in Au-Au collisions at 200 GeV—namely, (1) pion, kaon, proton, and Λ transverse momentum spectra, (2) the elliptic flow of many particle species, (3) the

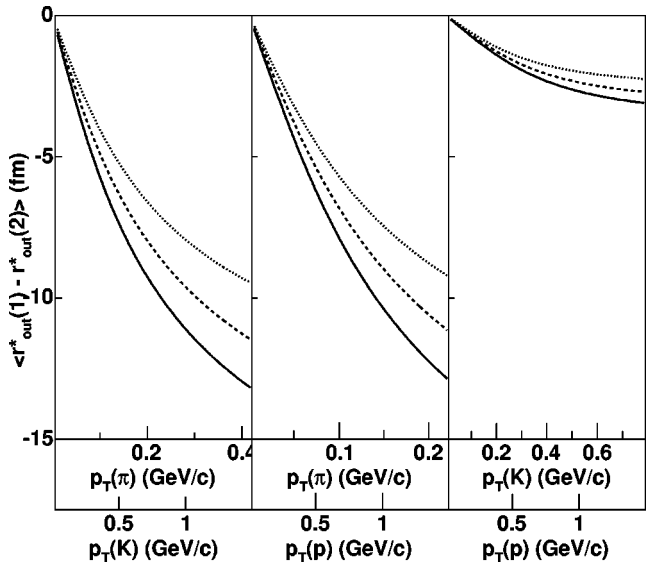

FIG. 55. Space-time separation between pions and kaons (left), pions and protons (middle), and kaons and protons (right) calculated with the best fit parameters in the three centrality bins. Solid line: parameters from fit to central data. Dashed line: parameters from midperipheral data. Dotted line: parameters from fit to peripheral data.

pion source radii including the oscillations with respect to the reaction plane, (4) the kaon source radii, and (5) the space-time separation between pion, kaon, and proton sources. If a satisfactory agreement between these various measurements is achieved, it would provide evidence of a collective expansion that would be very challenging to avoid.

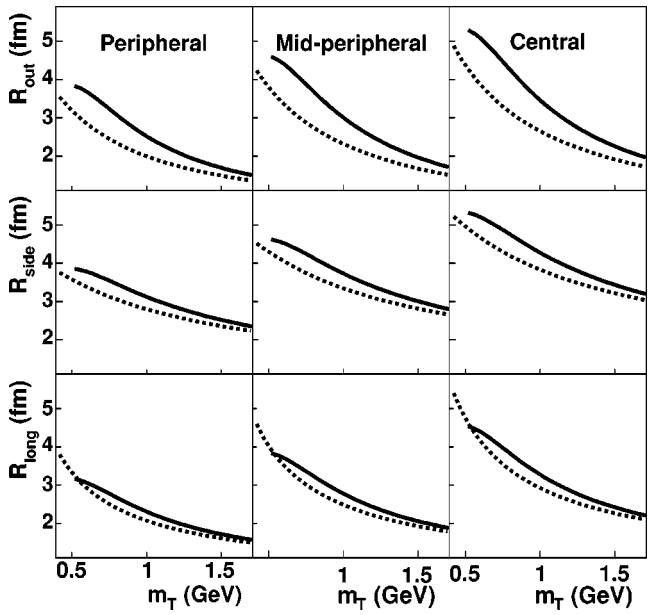

FIG. 56. Kaon source radii (solid line) compared to the pion radii (dashed line). The blast-wave calculations are performed with the best fit parameters in each centrality bins.

Furthermore, when high-quality data become available that allow for separate fits to each particle species, the blast-wave parametrization may prove to be an important and handy tool to assess whether or not the freeze-out time depends on the hadronic cross sections. It will be especially interesting to study particles with presumably low hadronic cross sections such as the ϕ, Ξ, and Ω. Since these particles may not be sensitive to hadronic collectivity, they may have a higher freeze-out temperature, and they may pick up less collective flow and freeze out earlier and from a smaller system than π, K, p, and Λ. It may be possible to distinguish between the collective expansion at the partonic (if any) versus hadronic stage.

V. SUMMARY AND OUTLOOK

We have discussed a scenario of particle kinetic freeze-out in heavy ion collisions, inspired by the results of full hydrodynamic calculations of the collision evolution. The scenario, while simplified, nevertheless includes several important features which drive experimental observables of the bulk properties of the system. This includes random ("thermal") motion superimposed upon collective flow fields, an anisotropic transverse geometry, and a freeze-out distribution in proper time. The main assumptions of the model are longitudinal boost invariance, the same parametric source for all particle types (e.g., π, p), and the invariance of source parameters over the kinetic freeze-out process (or, equivalently, that the model source parameters can represent the appropriate average of the time-evolving parameter). We discussed the interplay of the various features, such as space-momentum correlations depending on the competition between thermal and collective motion and the source geometry.

The various features (e.g., random thermal motion) were quantified with several parameters (e.g., T) in a mathematical model outlined in Sec. II. The general class of integrals which relate the model emission function to the various experimental observables was identified.

The sensitivity of several observables to the underlying physics represented by the parameters was studied by systematically varying each parameter in Sec. III. In addition to momentum-space observables such as the p_T spectra and elliptic flow, which have been discussed previously in the context of similar models, we focused on the sensitivity of final-state correlations between nonidentical particles and azimuthally sensitive HBT measurements, new coordinate-space-sensitive analysis tools now becoming available with the quality high-statistics data sets from RHIC.

The nontrivial interplay between competing physics effects was different for the different observables. It is clear that the model parameter space can only be constrained by examining several observables simultaneously; e.g., p_T spectra alone are insensitive to the source shape (R_y/R_x) and only crudely distinguish between high transverse flow and high temperature. Furthermore, from Sec. III, it is clear that experimental data can *overconstrain* the model parameter space. If consistency with p_T spectra and HBT data demand a high temperature and small transverse boost velocity, this has inescapable consequences for π-K correlations and elliptic flow. This allows for the "breakdown" of the parametric model and indicates the need to consider new driving physics effects.

In Sec. IV, the model was used as a functional form in a simultaneous fit to particle spectra $[(dN/dp_T)(p_T,m)]$, elliptic flow $[v_2(p_T,m)]$, and pion HBT radii $[R(p_T)]$ for three centrality classes from published RHIC results for Au-Au collisions at $\sqrt{s_{NN}}=130$ GeV. While higher-p_T HBT radii from PHENIX are only qualitatively described, a good fit is obtained to the p_T spectra, elliptic flow, and low-p_T STAR HBT radii.

Most of the physical parameter values obtained from the fits, as well as their evolution with collision centrality, fall within reasonable expectations. The exceptions are the evolution duration τ_0 and emission duration $\Delta\tau$, which are shorter than most physical models predict. The $\Delta\tau$ discrepancy may be partially resolved by an improved experimental treatment of the Coulomb interaction in HBT analyses; this will be evaluated upon publication of the new results from RHIC. The τ_0 value is strongly connected to the model assumption of boost invariance; if this assumption is invalid at midrapidity at RHIC (e.g., if there is longitudinal acceleration in the early system evolution), we expect our fit values to be only lower limits on the evolution duration.

Finally, Sec. IV discusses expectations for kaon HBT, azimuthally sensitive pion HBT, and emission space-time separations between nonidentical particles (π,K,p), based on the fit parameters to the published data. Expectations for the azimuthally sensitive pion HBT radii are driven by the elliptic flow data, which indicates $R_y > R_x$ (see Table II)—i.e., the freeze-out system shape is out-of-plane extended, qualitatively similar to the geometrical overlap configuration in the entrance channel of the collision. From Sec. III C, it is clear that this determines the phases (and amplitudes) of the expected oscillations in the HBT radii—i.e., the signs and magnitudes of $R^2_{\mu,2}$. If azimuthally sensitive HBT measurements confirm this out-of-plane freeze-out configuration, it might provide further evidence of short evolution times τ_0, since it would imply that the source, which is expanding faster in the reaction plane than out of it, did not have sufficient time to overcome its initial geometric anisotropy before freeze-out. Quantifying the time scale in this way is outside the scope of the blast-wave model, which does not attempt to describe the system evolution.

Exploration of simple parametrizations such as the blast wave is driven by the desire to connect observations to driving underlying physics. Furthermore, a quantitative interpretation of many measurements (perhaps especially two-particle interferometry) requires some model assumptions. Naturally, one prefers assumptions which are consistent with *other* measurements (e.g., elliptic flow) in the same system. Especially since first-principles model calculations have difficulty consistently explaining the range of observations in the soft sector of RHIC, it is hoped that insight may be gained from rather simple theory-*inspired* parametrizations such as the blast wave.

Inasmuch as such parametrizations reproduce observa

tions, there is hope that the driving physics effects have been approximately quantified, and one may compare the "underlying" parameters (e.g., time scales) with first-principles calculations in an effort to isolate the cause of the discrepancy between such calculations and observation. On the other hand, when simplistic parametrizations cannot, with any set of parameters, reproduce the main features of the data, it indicates that something additional is driving observations. In parametrizations, features may be implemented and "turned on and off," one at a time, testing for consistency with a *range* of experimental observations. The insight gained from such studies can then be fed back into more "theoretical" models. It is hoped that new experimental data will further constrain—or break—the simple parametrization, generating insights into the dynamics of heavy ion collisions at RHIC.

ACKNOWLEDGMENTS

We gratefully acknowledge fruitful discussions with Dr. J. Castillo, Dr. T. Csörgo, Dr. U. Heinz, Dr. P. Jacobs, Dr. P. Kolb, Dr. R. Lednicky, Dr. D. Magestro, Dr. R. L. Ray, Dr. R. Snellings, Dr. B. Tomášik, Dr. S. Voloshin, Dr. R. Wells, and Dr. U. Wiedemann. We thank Dr. D. Magestro, Dr. K. Schweda, and Dr. P. Sorensen for a careful reading of an early version of the text. This work was supported by the U.S. National Science Foundation under Grant No. PHY-0099476 and by the U.S. Department of Energy under Contract No. DE-AC03-76SF00098.

[1] For reviews and recent developments, see proceedings of the Quark Matter conferences: *QM99* [Nucl. Phys. **A661**, 1 (1999)]; *QM01* [Nucl. Phys. **A698**, 1 (2002)]; *QM02* [Nucl. Phys. **A715**, 1 (2003)].
[2] E. V. Shuryak, Phys. Lett. **78B**, 150 (1978).
[3] E. V. Shuryak, Sov. J. Nucl. Phys. **28**, 408 (1978); J. Kapusta, P. Lichard, and D. Seibert, Phys. Rev. D **44**, 2774 (1991).
[4] BRAHMS Collaboration, Phys. Rev. Lett. **91**, 072305 (2003); PHENIX Collaboration, *ibid.* **87**, 052301 (2001); nucl-ex/0207009; Phys. Rev. Lett. **91**, 072301 (2003); , Phys. Rev. Lett. **91**, 072303 (2003); Phys. Rev. C **69**, 034910 (2004); PHOBOS Collaboration, Phys. Rev. Lett. **91**, 072302 (2003); STAR Collaboration, *ibid.* **89**, 202301 (2002); **90**, 032301 (2003); **90**, 082302 (2003); **91**, 172302 (2003); **91**, 072304 (2003).
[5] R. Baier, D. Schiff, and B. G. Zakharov, Annu. Rev. Nucl. Part. Sci. **50**, 37 (2000); M. Gyulassy, I. Vitev, X. N. Wang, and B. Zhang, nucl-th/0302077.
[6] U. A. Wiedemann and U. Heinz, Phys. Rep. **319**, 145 (1999); U. Heinz and B. V. Jacak, Annu. Rev. Nucl. Part. Sci. **49**, 529 (1999).
[7] R. Haburry-Brown and R. Q. Twiss, Nature (London) **177**, 27 (1956); **178**, 1046 (1960).
[8] S. Soff, S. Bass, D. Hardtke, and S. Panitkin, Nucl. Phys. **A715**, 801 (2003).
[9] U. Heinz and P. F. Kolb, Nucl. Phys. **A702**, 269 (2002); hep-ph/0111075.
[10] K. Morita, S. Muroya, C. Nonaka, and T. Hirano, Phys. Rev. C **66**, 054904 (2002).
[11] T. Hirano and K. Tsuda, Phys. Rev. C **66**, 054905 (2002).
[12] B. Zhang, C. M. Ko, B. A. Li, and Z. W. Lin, Phys. Rev. C **61**, 067901 (2000); Z. W. Lin, S. Pal, C. M. Ko, B. A. Li, and B. Zhang, *ibid.* **64**, 011902 (2001).
[13] Especially after so-called "nonflow" contributions [14] are removed from the experimental data, AMPT requires parton cross sections $\sigma \lesssim 3$ mb to reproduce STAR elliptic flow data [15] and $\sigma \approx 10$ mb to reproduce HBT data. We thank Zi-wei Lin for bringing this to our attention.
[14] STAR Collaboration, C. Adler *et al.*, Phys. Rev. C **66**, 034904 (2002).
[15] Z. W. Lin and C. M. Ko, Phys. Rev. C **65**, 034904 (2002).
[16] Z. W. Lin, C. M. Ko, and S. Pal, Phys. Rev. Lett. **89**, 152301 (2002).
[17] M. Csanád, T. Csörgő, and B. Lörstad, nucl-th/0310040; M. Csanád, T. Csörgő, B. Lörstad, and A. Ster, Acta Phys. Pol. B **35**, 191 (2004).
[18] P. Huovinen, P. F. Kolb, U. Heinz, P. V. Ruuskanen, and S. Voloshin, Phys. Lett. B **503**, 58 (2001).
[19] H. Sorge, Phys. Rev. Lett. **78**, 2309 (1997).
[20] T. Humanic, nucl-th/0203004; Nucl. Phys. **A715**, 641c (2003).
[21] D. Molnar and M. Gyulassy, Nucl. Phys. **A698**, 379 (2002); Phys. Rev. Lett. **92**, 052301 (2004).
[22] S. Bass, B. Mueller, and D. Srivastava, Phys. Lett. B **551**, 277 (2003).
[23] U. Heinz and P. F. Kolb, Phys. Lett. B **542**, 216 (2002).
[24] D. Teaney, J. Lauret, and E. Shuryak, nucl-th/0110037.
[25] D. Teaney, nucl-th/0301099.
[26] H. G. Fischer, Nucl. Phys. **A715**, 118c (2003).
[27] Y. V. Kovchegov and K. L. Tuchin, Nucl. Phys. **A708**, 413 (2002); **A717**, 249 (2003).
[28] T. Peitzmann, nucl-th/0303046.
[29] J. M. Burward-Hoy for the PHENIX Collaboration, Nucl. Phys. **A715**, 498 (2003).
[30] T. Peitzmann, Eur. Phys. J. C **26**, 539 (2003).
[31] B. Tomasik, in proceedings of 38 Rencontres de Moriond, QCD and hadronic interactions, nucl-th/0304079.
[32] G. D. Westfall, J. Gosset, P. J. Johansen, A. M. Poskanzer, W. G. Meyer, H. H. Gutbrod, A. Sandoval, and R. Stock, Phys. Rev. Lett. **37**, 1202 (1976).
[33] J. P. Bondorf, S. I. A. Garpman, and J. Zimanyi, Nucl. Phys. **A296**, 320 (1978).
[34] P. J. Siemens and J. O. Rasmussen, Phys. Rev. Lett. **42**, 880 (1979).
[35] E. Schnedermann, J. Sollfrank, and U. Heinz, Phys. Rev. C **48**, 2462 (1993).
[36] J. D. Bjorken, Phys. Rev. D **27**, 140 (1983).
[37] STAR Collaboration, C. Adler *et al.*, Phys. Rev. Lett. **87**, 182301 (2001).
[38] STAR Collaboration, F. Retière *et al.*, nucl-ex/0111013.
[39] U. A. Wiedemann, Phys. Rev. C **57**, 266 (1998).

[40] B. Tomášik, U. A. Wiedemann, and U. Heinz, Nucl. Phys. **A663**, 753 (2000); B. Tomášik and U. Heinz, Phys. Rev. C **65**, 031902 (2002).
[41] U. Heinz and S. H. M. Wong, Phys. Rev. C **66**, 014907 (2002).
[42] We thank Sergei Voloshin for correcting an error we had previously made in deriving Eq. (6).
[43] S. V. Akkelin and Yu. M. Sinyukov, Phys. Lett. B **356**, 525 (1995).
[44] U. A. Wiedemann, P. Scotto, and U. Heinz, Phys. Rev. C **53**, 918 (1996).
[45] T. Csörgő and B. Lörstad, Phys. Rev. C **54**, 1390 (1996).
[46] Y.-F. Wu, U. Heinz, B. Tomášik, and U. Wiedemann, Eur. Phys. J. C **1**, 599 (1998).
[47] Since particle emission occurs only after the collision begins (i.e., when $\tau > 0$), the lower limit on the τ integration in Eqs. (15) and (16) ought to be zero instead of $-\infty$. This distinction vanishes if $\Delta\tau \ll \tau_0$, and the effect is negligible for the range of parameter values explored here.
[48] S. A. Voloshin and A. M. Poskanzer, Phys. Lett. B **474**, 27 (2000).
[49] S. A. Voloshin, Nucl. Phys. **A715**, 379c (2003); nucl-th/0202072.
[50] S. A. Voloshin, Phys. Rev. C **55**, R1630 (1997).
[51] P. Houvinen, P. F. Kolb, and U. Heinz, Nucl. Phys. **A698**, 475c (2002).
[52] E. V. Shuryak, Phys. Rev. C **66**, 027902 (2002).
[53] R. Lednický, V. I. Lyuboshitz, B. Erazmus, and D. Nouais, Phys. Lett. B **373**, 30 (1996).
[54] S. Pratt, T. Csörgő, and J. Zimanyi, Phys. Rev. C **42**, 2646 (1990); G. Bertsch, M. Gong, and M. Tohyama, *ibid.* **37**, 1896 (1988).
[55] U. Heinz, A. Hummel, M. A. Lisa, and U. A. Wiedemann, Phys. Rev. C **66**, 044903 (2002).
[56] M. A. Lisa, U. Heinz, and U. A. Wiedemann, Phys. Lett. B **489**, 287 (2000).
[57] E895 Collaboration, M. A. Lisa *et al.*, Phys. Lett. B **496**, 1 (2000).
[58] T. Csörgő, S. V. Akkelin, Y. Hama, B. Lukács, and Yu. M. Sinyukov, Phys. Rev. C **67**, 034904 (2003).
[59] Phenix Collaboration, K. Adcox *et al.*, Phys. Rev. Lett. **88**, 192302 (2002).
[60] A. N. Makhlin and Yu. M. Sinyukov, Z. Phys. C **39**, 69 (1988).
[61] M. Herrmann and G. F. Bertsch, Phys. Rev. C **51**, 328 (1995).
[62] Yu. M Sinyukov, in *Hot Hadronic Matter: Theory and Experiment*, edited by J. Rafelski, Vol. 346 of *NATO Advanced Study Institute, Series B: Physics* (Plenum, New York, 1995), p. 309.
[63] D. Hardtke and S. Voloshin, Phys. Rev. C **61**, 024905 (2000).
[64] D. Brown and P. Danielewicz, Phys. Rev. C **64**, 014902 (2001); P. Danielewicz, D. A. Brown, M. Heffner, S. Pratt, and R. Soltz, nucl-th/0407022.
[65] S. Nickerson, T. Csörgő, and D. Kiang, Phys. Rev. C **57**, 3251 (1998).
[66] U. Wiedemann and U. Heinz, Phys. Rev. C **56**, 3265 (1997).
[67] D. Magestro (private communication). Model as described in P. Braun-Munzinger, K. Redlich, and J. Stachel, nucl-th/0304013.
[68] T. Csörgő, B. Lörstad, and J. Zimányi, Z. Phys. C **71**, 491 (1996).
[69] D. H. Rischke and M. Gyulassy, Nucl. Phys. **A608**, 479 (1996); D. H. Rischke, *ibid.* **A610**, 88c (1996).
[70] STAR Collaboration, C. Adler *et al.*, Phys. Rev. Lett. **87**, 082301 (2001).
[71] P. Kolb and D. Magestro (private communication).
[72] R. Lednický, nucl-th/0305027; Proceedings of CIPPQG'01, nucl-th/0112011; Proceedings of XXXII ISMD, nucl-th/0212089.
[73] S. Voloshin, R. Lednický, S. Panitkin, and N. Xu, Phys. Rev. Lett. **79**, 4766 (1997).
[74] D. Ardouin *et al.*, Phys. Lett. B **446**, 191 (1999).
[75] C. Greiner, P. Koch, and H. Stöcker, Phys. Rev. Lett. **58**, 1825 (1987); B. Lukács, J. Zimányi, and N. L. Balazs, Phys. Lett. B **183**, 27 (1987); M. Gyulassy, *ibid.* **286**, 211 (1992).
[76] STAR Collaboration, F. Retière, Nucl. Phys. **A715**, 591c (2003).
[77] STAR Collaboration, J. Adams *et al.*, Phys. Rev. Lett. **91**, 262302 (2004).
[78] R. Lednický, in Proceedings of the 8th International Workshop on Multiparticle Production, Correlations and Fluctuations, 1998, nucl-th/0304063; R. Lednický, S. Panitkin, and N. Xu, nucl-th/0304062.
[79] B. Back *et al.*, nucl-ex/0406021.
[80] J. Adams *et al.*, Phys. Rev. Lett. **92**, 112301 (2004).
[81] K. Adcox *et al.*, Phys. Rev. Lett. **88**, 242301 (2002).
[82] C. Adler *et al.*, Phys. Rev. Lett. **89**, 092301 (2002).
[83] N. Xu and M. Kaneta, Nucl. Phys. **A698**, 306c (2002).
[84] P. Kolb, in Proceedings for the 19th Winter Workshop on Nuclear Dynamics, nucl-th/0304036.
[85] T. Hirano and K. Tsuda, Phys. Rev. C **66**, 041901 (2002).
[86] T. Csörgő and L. P. Csernai, Phys. Lett. B **333**, 494 (1994).
[87] STAR Collaboration, M. López-Noriega *et al.*, Nucl. Phys. **A715**, 623c (2003).
[88] PHENIX Collaboration, A. Enokizono *et al.*, Nucl. Phys. **A715**, 595c (2003).